# 3 Specular Reflection Spectroscopy

Robert J. Lipert, Brian D. Lamp, and Marc D. Porter

## 3.1 INTRODUCTION

This chapter on specular reflection spectroscopy focuses on applications in the mid-infrared region of the spectrum. Applications in other spectral regions or using other spectroscopic techniques, such as Raman spectroscopy, generally follow similar patterns as discussed in this chapter.

In the past few decades, infrared spectroscopy (IRS) has developed into an invaluable diagnostic tool for unraveling details about the bonding and molecular structure at surfaces [1, 2, 3, 4, 5, 6]. The importance of IRS derives from five major factors, The first and most critical factor is the role of interfacial phenomena in a vast number of emerging material and surface technologies. Examples include adhesion, catalysis, tribology, microelectronics, and electrochemistry [3, 7, 8, 9]. The second factor stems from the

information-rich content of an IRS spectrum of a surface. That is, the frequencies of the spectroscopic features can be used to identify the chemical composition of a surface and the magnitudes and polarization dependencies of the features used to determine average structural orientations. The third factor arises from advances in the performance of IRS instrumentation. The most important of these advancements are the high throughput and multiplex advantages of Fourier transform interferometry, the development of high sensitivity, low-noise IR detectors, and the improvement in the computational rates of personal computers and their adaptation to the operation of chemical instrumentation. The fourth factor results from the compatibility of IRS with a variety of sample environments. This situation opens the door to a wide range of *in situ* studies, including characterizations in high-pressure environments and in condensed phases. The fifth factor rests with the application of classical electromagnetic theory to IRS characterizations in a reflection mode. Such considerations provide a basis to delineate the experimental conditions requisite for optimal detection as well as to separate shifts and distortions of spectral bands induced by optical effects from those due to bonding and surface-induced structural changes.

As is evident from the general theme of this monograph, there are many different experimental modes for probing the composition and structure of interfaces with infrared spectroscopy. This chapter focuses on the application of infrared spectroscopy to the characterization of smooth surfaces. We define smooth surfaces as those that can be generally described as having a "mirrorlike" or specular finish, that is to say, surfaces with irregularities that are small in comparison to the wavelength of incident light. Armed with this definition, an overview of the reflection experiment within the context of classical electromagnetic theory is presented in the following section. We then utilize the formulations from these considerations to gain insight into the dependence of the reflection spectrum on the optical properties of the film, substrate, surrounding medium, and on the angle of incidence and polarization of the incoming radiation. This section is followed by a discussion of various experimental approaches for the collection of a reflection spectrum at a specular surface, an approach often referred to as IRS in a specular, external, or reflection-absorption mode (Fig. 3.1). This chapter concludes with brief descriptions of recent applications selected to demonstrate the overall utility of this technique.

## 3.2   THEORETICAL CONSIDERATIONS

Considerable insight has been gained in describing the phenomena associated with specular reflectance spectroscopy using classical electrodynamic theory [10, 11, 12, 13]. In this section we will first develop the wave
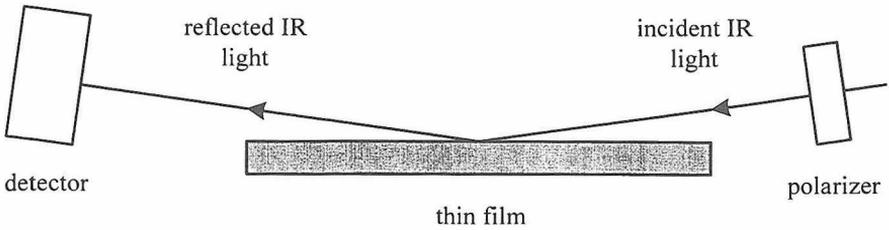
reflected IR
light

incident IR
light

detector

thin film

polarizer

**Fig. 3.1** Schematic diagram for a specular reflectance measurement.

equations for the propagation of light in both transparent and absorbing media. We will then consider the effects on a reflection measurement that occur when light encounters an interface of differing optical properties. Since the absorption of light by a modified surface is proportional to the mean-square electric fields at the interface, insights into the factors that effect these fields foster an understanding of the conditions optimal for the detection of coatings at different types of reflective substrates. We will also show how the optical properties of the film and substrate can give rise to shifts and distortions of the spectral band shapes of the modifying film and how considerations of such spectra can be exploited to obtain orientational information about the modifying film.

### Propagation of Electromagnetic Radiation through a Nonconducting Homogeneous Medium

For electromagnetic radiation propagating through a transparent uniform isotropic medium, manipulation of Maxwell's equations results in the following expression for the electric field vector $\mathbf{E}$ [14]:

$$\nabla^2 \mathbf{E} = \frac{\varepsilon \mu_p}{c^2} \frac{\partial^2 \mathbf{E}}{\partial t^2}. \tag{3.1}$$

In this expression $\nabla^2$ is the Laplacian operator, $\varepsilon$ is the dielectric constant of the medium, $\mu_p$ is the relative magnetic permeability of the medium, $c$ is the speed of light, and $t$ is time. Equation (3.1) has the form of the classical wave equation

$$\nabla^2 f = \frac{1}{v^2} \frac{\partial^2 f}{\partial t^2} \tag{3.2}$$

where $f$ is the function that describes the wave and $v$ is its velocity. The

velocity of the electromagnetic wave is therefore

$$v = \frac{c}{\sqrt{\varepsilon \mu_p}} \tag{3.3}$$

The plane traveling wave solution to (3.1) is given by

$$\hat{\mathbf{E}} = E^0 \exp[i(\mathbf{K} \cdot \mathbf{r} - \omega t)], \tag{3.4}$$

where $E^0$ is the maximum amplitude of the electromagnetic wave, $\mathbf{r}$ is the vector distance from the origin to the point of measurement, $\mathbf{K}$ is the propagation vector with units of inverse length, $\omega = 2\pi v = 2\pi c/\lambda$ and is the angular frequency with units of rad/s, and $v$ and $\lambda$ are the frequency and vacuum wavelength, respectively, of the electromagnetic radiation. Substituting (3.4) into (3.1) shows that

$$K = (\varepsilon \mu_p)^{1/2} \left(\frac{\omega}{c}\right) = (\varepsilon \mu_p)^{1/2} \left(\frac{2\pi v}{c}\right) = (\varepsilon \mu_p)^{1/2} \left(\frac{2\pi}{\lambda}\right). \tag{3.5}$$

In a nonmagnetic medium, $\mu_p \cong 1.0$. Also the refractive index $n$ of a medium is given by ratio of the velocity of light in the medium to the velocity in vacuum, namely $n = c/v$. Thus we see from (3.3) that

$$n = (\varepsilon)^{1/2}. \tag{3.6}$$

Combining and rearranging (3.4), (3.5) and (3.6) gives

$$\hat{\mathbf{E}} = E^0 \exp\left[ i\left(\frac{2\pi n}{\lambda} \mathbf{s} \cdot \mathbf{r} - \omega t\right)\right], \tag{3.7}$$

where $\mathbf{s}$ is a unit vector in the direction of propagation.

In an absorbing medium, as depicted in Fig. 3.2, the plane traveling wave undergoes an exponential attenuation with increasing propagation distance. The electric field vector can then be represented as

$$\hat{\mathbf{E}} = E^0 \exp\left[ i\left(\frac{2\pi n}{\lambda} \mathbf{s} \cdot \mathbf{r} - \omega t\right)\right] \exp\left(-\frac{2\pi k}{\lambda} \mathbf{s} \cdot \mathbf{r}\right), \tag{3.8}$$

where $k$ is referred to as the absorption index or extinction coefficient [13]. This $k$ can be related to the absorption coefficient $\alpha$ of Lambert's law, which describes the attenuation of the intensity of light as it propagates through an absorbing medium. Neglecting reflection at the surface of the absorbing
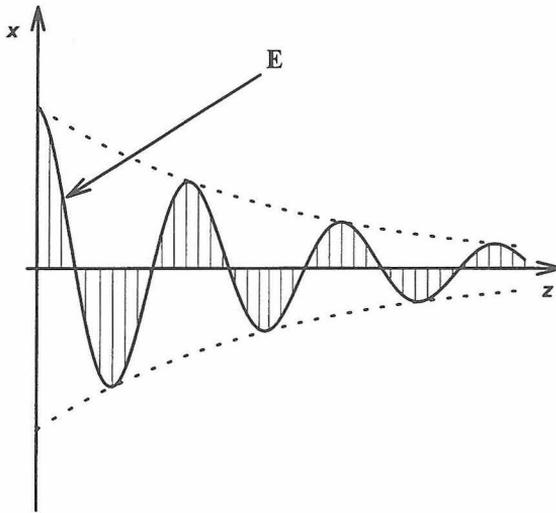
**Fig. 3.2** Propagation of an electromagnetic wave into an absorbing medium ($z$-direction).

medium, the Lambert law is given by

$$I = I^0 \exp(-\alpha z), \tag{3.9}$$

where $I^0$ is the initial radiation intensity and $z$ is the distance of propagation into the absorbing medium. The radiation intensity, $I$, is proportional to the mean-square electric field. Therefore $I$ is proportional to $\exp\left(-\dfrac{4\pi k}{\lambda} \mathbf{s} \cdot \mathbf{r}\right)$ and thus

$$\alpha = \frac{4\pi k}{\lambda}. \tag{3.10}$$

It is therefore possible to obtain $k$ for a medium from a transmission spectrum of a thin film of the material.

If we define a complex refractive index as

$$\hat{n} = n + ik, \tag{3.11}$$

Equation (3.8) can be recast into the form of (3.7) with $\hat{n}$ replacing $n$:

$$\hat{\mathbf{E}} = E^0 \exp\left[i\left(\frac{2\pi\hat{n}}{\lambda} \mathbf{s} \cdot \mathbf{r} - \omega t\right)\right]. \tag{3.12}$$

The complex refractive index of a medium is related to its complex dielectric constant by

$$\hat{n} = (\hat{\varepsilon})^{1/2}. \tag{3.13}$$

Therefore,

$$\hat{\varepsilon} = \hat{n}^2 = n^2 + i2nk - k^2 = \varepsilon' + i\varepsilon'', \tag{3.14}$$

where

$$\varepsilon' = n^2 - k^2 \qquad \varepsilon'' = 2nk. \tag{3.15}$$

In general, $\hat{n}$ or $\hat{\varepsilon}$ are functions of the radiation frequency. We can therefore write

$$\hat{n}(\bar{v}) = n(\bar{v}) + ik(\bar{v}) \quad \text{and} \quad \hat{\varepsilon}(\bar{v}) = \varepsilon'(\bar{v}) + i\varepsilon''(\bar{v}), \tag{3.16}$$

where $\bar{v} = 1/\lambda$ and has the units of wavenumber. These functions completely describe the optical properties of a medium. For example, the complex refractive index $\hat{n}$ describes both refraction, through $n$, and absorption, through $k$, of light by the medium. Importantly, the real and imaginary parts of these optical functions are not independent but are related through the Kramers-Kronig transformation. Using the refractive index as an example, the real part of the refractive index at $\bar{v} = \bar{v}_i$ can be calculated from $k(\bar{v})$ using the following expression [15]:

$$n(\bar{v}_i) = n_\infty + \frac{2}{\pi} P \int_0^\infty \frac{\bar{v}k(\bar{v})}{(\bar{v}^2 - \bar{v}_i^2)} d\bar{v}. \tag{3.17}$$

In this equation the constant $n_\infty$ represents the contribution to the refractive index of regions far removed from any absorption band and $P$ indicates that the Cauchy principal value of the integral must be taken because of the singularity at $\bar{v} = \bar{v}_i$. In practice, measurements are performed across an absorption band from $\bar{v}_a$ to $\bar{v}_b$. The transformation is then usually approximated as

$$n(\bar{v}_i) = \bar{n} + \frac{2}{\pi} P \int_{\bar{v}_a}^{\bar{v}_b} \frac{\bar{v}k(\bar{v})}{(\bar{v}^2 - \bar{v}_i^2)} d\bar{v}, \tag{3.18}$$

where $\bar{n}$ is either the baseline refractive index or the mean refractive index across the band [15]. As was noted earlier, the function $k(\bar{v})$ can be obtained from an absorption spectrum of a thin film.

### Reflection of Electromagnetic Radiation at a Boundary between Homogeneous Media of Different Optical Properties

*Reflectivity*

The optical effects that arise when recording absorption spectra using specular reflection can have a large impact on the magnitudes and shapes of the spectra. To interpret the absorption spectra obtained using a specular reflectance geometry, we must understand the influence of the optical constants of the media on the electric fields at the reflecting interfaces. It will be shown that when an absorption band is present in a medium, not only is the light intensity affected by absorption but also by changes in the reflectivity of the interface. That is, the intensity of the reflected light is affected by changes in $n$ as well as changes in $k$ across the absorption band. Changes in reflectivity across an absorption band can result in a distortion of the band shape and a shifting of the measured absorption maximum, compared to a thin film transmission spectrum. In addition, because of the phase shift in the light that occurs upon reflection, the mean-square electric fields present near an interface are dependent on the polarization of the incident radiation. This situation gives rise to a surface effect, often referred to as the *surface selection rule*, that can be used to obtain information on the structural orientation of modifying films [10, 16].

The development of the equations for the electric fields present in a three-phase, optically isotropic medium [10] treats the system as a series of planar, parallel optical boudaries. Figure 3.3 presents a schematic of this model. In general, the propagating radiation can pass through $n$ phases, with the optical functions of phase $j$ given by

$$\hat{n}_j = n_j + ik_j. \tag{3.19}$$

Reflection occurs at the boundary between phases. It is usually the case that phase 1 is air (i.e., $n \approx 1.0$, $k_1 \approx 0$), phase 2 is the sample thin film, and phase 3 is a supporting medium of effectively infinite thickness. The $z$-direction is normal to the interfaces with the positive direction extending into phase 2 from phase 1. The degree to which radiation is reflected or transmitted at an interface depends on the polarization and angle of incidence of the incoming radiation as well as the optical functions of the two adjacent phases. Parallel-polarized ($p$-polarized) light is polarized in the plane of incidence and has $x$- and $z$-components, and perpendicular-polarized ($s$-polarized) light has only a $y$-component. The reflectivity of the interface between phases $j$ and $k$, $R_{jk}$, is given by the Fresnel coefficients for reflection, $r_{jk}$ [17, 18]:

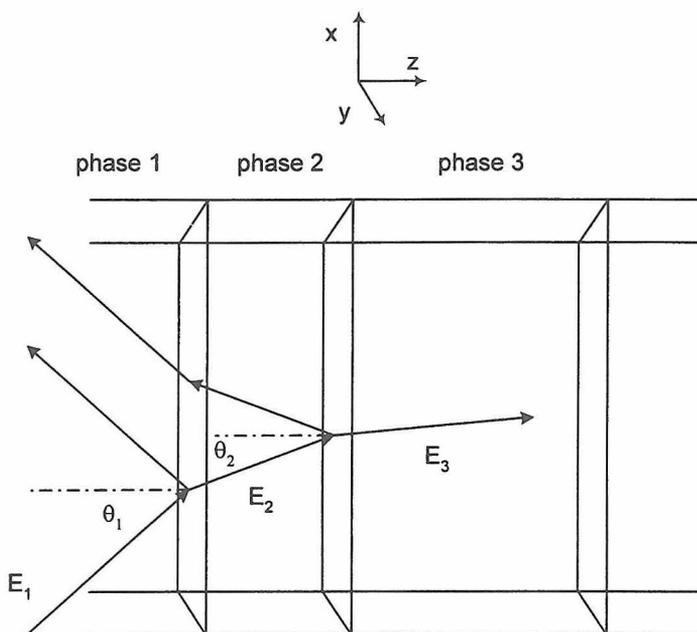$$R_{jk} = |r_{jk}|^2 = r_{jk}r_{jk}^*. \tag{3.20}$$

**Fig. 3.3**  Electric field vectors for plane-polarized light incident on a three-phase medium. The plane of polarization is the x-z plane.

The Fresnel coefficients are defined as the ratios of the complex amplitudes of the electric field vectors of the incident waves to those of the reflected waves. Similarly the intensity of transmitted light is given by the Fresnel coefficients for transmission, $t_{jk}$, which are the ratios of the complex amplitudes of the electric field vectors of the incident waves to those of the transmitted waves. Both sets of coefficients are obtained from Maxwell's equations by applying the continuity requirements for $\hat{E}$ and $\hat{H}$ across the phase boundaries. To simplify the expressions for $r_{jk}$, it is customary to define a refractive coefficient for phase $j$ as

$$\xi_j = \hat{n}_j \cos \hat{\theta}_j, \tag{3.21}$$

where $\hat{n}_j$ and $\hat{\theta}_j$ are the complex refractive index and complex angle of incidence, respectively, in phase $j$ [11]. The Fresnel coefficients for reflection and transmission of radiation polarized perpendicular and parallel to the plane of incidence are then given by

$$r_{\perp jk} = \frac{\xi_j - \xi_k}{\xi_j + \xi_k}, \tag{3.22}$$

$$t_{\perp jk} = \frac{2\xi_j}{\xi_j + \xi_k}, \tag{3.23}$$

$$r_{\parallel jk} = \frac{\hat{n}_k^2 \xi_j - \hat{n}_j^2 \xi_k}{\hat{n}_k^2 \xi_j + \hat{n}_j^2 \xi_k}, \tag{3.24}$$

$$t_{\parallel jk} = \frac{2\hat{n}_j \hat{n}_k \xi_j}{\hat{n}_k^2 \xi_j + \hat{n}_j^2 \xi_k}. \tag{3.25}$$

Thus the reflectivities at the interface between phases 1 and 2 for the two polarizations are

$$R_{\perp 12} = \left| \frac{\xi_1 - \xi_2}{\xi_1 + \xi_2} \right|^2, \tag{3.26}$$

$$R_{\parallel 12} = \left| \frac{\hat{n}_2^2 \xi_1 - \hat{n}_1^2 \xi_2}{\hat{n}_2^2 \xi_1 + \hat{n}_1^2 \xi_2} \right|^2. \tag{3.27}$$

It is instructive to evaluate the reflectivity for the ideal case where the incident light is normal to the phase boundary, phase 1 is air, and phase 2 is a very strongly absorbing medium whose refractive index can be approximated as purely imaginary. This situation is similar to the reflection of infrared radiation at a metal surface [19]. In this example, $\theta_1 = 0$, $\xi_1 = 1$, and $\xi_2 = ik$. The reflectivity then becomes

$$R = \frac{(1 - ik)(1 + ik)}{(1 + ik)(1 - ik)} = 1. \tag{3.28}$$

We therefore see that metals are highly efficient reflectors of infrared radiation because of their very strong absorption of the incident light. This situation arises from the high density of the free electron gas of metals, which strongly absorbs infrared radiation and results in a highly efficient reflection of the incident beam.

For the common situation of a three-phase system (e.g., the case where an organic film is supported on a smooth substrate and is in contact with the ambient environment), the perpendicular and parallel Fresnel coefficients $r_{123}$ are

$$r_{\perp} = \frac{r_{\perp 12} + r_{\perp 23} e^{-2i\beta}}{1 + r_{\perp 12} r_{\perp 23} e^{-2i\beta}}, \tag{3.29}$$

$$r_{\parallel} = \frac{r_{\parallel 12} + r_{\parallel 23} e^{-2i\beta}}{1 + r_{\parallel 12} r_{\parallel 23} e^{-2i\beta}}, \tag{3.30}$$

where $\beta$ represents the attenuation of the beam as it travels through phase 2 of thickness $d$ and is given by

$$\beta = 2\pi \frac{d}{\lambda} \xi_2. \tag{3.31}$$

When calculating the electric field at an interface at which reflection is occurring, it is also necessary to take into account the phase change in the electric field that occurs upon reflection. This phase change, $\delta^r_{jk}$, is given by the real and imaginary parts of the Fresnel coefficients as follows:

$$\delta^r_{jk} = \arg(r_{jk}) = \tan^{-1}\left[\frac{\mathrm{Im}(r_{jk})}{\mathrm{Re}(r_{jk})}\right], \tag{3.32}$$

where $\arg(r_{jk})$ is the angle that is the argument of the complex number $r_{jk}$. By convention, when the electric field vectors for incident and reflected light are antiparallel and equal in magnitude, $\delta^r_{\perp} = -180$ and $\delta^r_{\parallel} = 0$ [20]. The reflectivity of a three-phase system is then [11]

$$R_{\perp} = \frac{R_{\perp 12} + R_{\perp 23}e^{-4\mathrm{Im}\beta} + R^{1/2}_{\perp 12}R^{1/2}_{\perp 23}e^{-2\mathrm{Im}\beta}2\cos(\delta^r_{\perp 23} - \delta^r_{\perp 12} + 2\mathrm{Re}\beta)}{1 + R_{\perp 12}R_{\perp 23}e^{-4\mathrm{Im}\beta} + R^{1/2}_{\perp 12}R^{1/2}_{\perp 23}e^{-2\mathrm{Im}\beta}2\cos(\delta^r_{\perp 23} + \delta^r_{\perp 12} + 2\mathrm{Re}\beta)}. \tag{3.33}$$

The same expression holds for parallel polarization, which, with appropriate substitutions, is

$$R_{\parallel} = \frac{R_{\parallel 12} + R_{\parallel 23}e^{-4\mathrm{Im}\beta} + R^{1/2}_{\parallel 12}R^{1/2}_{\parallel 23}e^{-2\mathrm{Im}\beta}2\cos(\delta^r_{\parallel 23} - \delta^r_{\parallel 12} + 2\mathrm{Re}\beta)}{1 + R_{\parallel 12}R_{\parallel 23}e^{-4\mathrm{Im}\beta} + R^{1/2}_{\parallel 12}R^{1/2}_{\parallel 23}e^{-2\mathrm{Im}\beta}2\cos(\delta^r_{\parallel 23} + \delta^r_{\parallel 12} + 2\mathrm{Re}\beta)}. \tag{3.34}$$

We note that equations (3.33) and (3.34) can be viewed conceptually as the reflection analogs to the Beer-Lambert law for transmission spectroscopy.

### Mean-Square Electric Fields

The change in the intensity of the reflected light because of absorption by a thin film is proportional to the mean-square electric field, $\langle E^2 \rangle$, in the thin film. For insight into the differences between infrared absorption spectra of free-standing thin films and reflection spectra of thin films supported on a reflective surface, it is worthwhile to examine the mean-square electric fields in each of the phases that constitute the reflecting stratified medium.

The electric fields of incident and specularly reflected light add vectorially to produce a standing-wave electric field in each phase except the last phase. Because a standing wave is formed above a reflecting surface, the mean-square electric fields vary with distance from the reflecting surface and are different for parallel and perpendicular polarizations. With the relationships derived above, the expressions for the mean-square fields for the various polarization components in phase 1, relative to the incident mean-square field ($\langle E_1^{ot2} \rangle$), are given by [11]

$$\frac{\langle E_{\perp 1}^2 \rangle}{\langle E_{\perp 1}^{ot2} \rangle} = (1 + R_\perp) + 2R_\perp^{1/2} \cos\left[ \delta_\perp^r - 4\pi \left(\frac{z}{\lambda}\right) \xi_1 \right], \tag{3.35}$$

$$\frac{\langle E_{\parallel 1x}^2 \rangle}{\langle E_{\parallel 1x}^{ot2} \rangle} = \cos^2 \theta_1 \left\{ (1 + R_\parallel) - 2R_\parallel^{1/2} \cos\left[ \delta_\parallel^r - 4\pi \left(\frac{z}{\lambda}\right) \xi_1 \right] \right\}, \tag{3.36}$$

$$\frac{\langle E_{\parallel 1z}^2 \rangle}{\langle E_{\parallel 1z}^{ot2} \rangle} = \sin^2 \theta_1 \left\{ (1 + R_\parallel) + 2R_\parallel^{1/2} \cos\left[ \delta_\parallel^r - 4\pi \left(\frac{z}{\lambda}\right) \xi_1 \right] \right\}. \tag{3.37}$$

Plots of the reflectivity, phase change, and mean-square electric fields at $2000 \, \text{cm}^{-1}$ are shown for various two-phase systems in Fig. 3.4 as a function of $\theta_1$. The optical constants for the different media used in the calculations are given in Table 3.1. The selected surfaces — gold, glassy carbon, glass, and silicon — illustrate the effect of varying optical constants on the reflective properties of materials often encountered in a specular reflection characterization. We see that because gold has a high reflectivity for both polarizations at nearly all angles of incidence, the $x$- and $y$-components of the mean-square electric fields at the gold surface have negligibly small values at all angles of incidence. However, the $z$-component of the mean-square electric field at the gold surface has a significant intensity, with a maximum

TABLE 3.1  Optical Constants Used for Calculating the Optical Properties of the Various Media

| Medium | $n$ | $k$ |
| --- | --- | --- |
| Air | 1.0 | 0.0 |
| Gold[a] | 2.7 | 28.5 |
| Glassy carbon[a] | 2.9 | 1.3 |
| SiO$_2$ (glass)[b] | 1.342 | 0.0 |
| Si[b] | 3.426 | 0.0 |

*Note:* Values of $n$ and $k$ are valid for $2000 \, \text{cm}^{-1}$ radiation.
[a]See [22].
[b]See [19].

that is nearly a factor of four stronger than the incident field when $\theta_1$ is slightly less than 80°. It is the difference in the intensities of the electric field components that gives rise to the surface effect that is exploited to determine the spatial orientation of the modifying film (see below).

In contrast to gold, glassy carbon, which has a similar $n$ to gold but is a much weaker absorber of infrared radiation (i.e., a smaller $k$), has a much lower reflectivity, and hence the $z$-component of the mean-square electric field at the surface is smaller. In this case the maximum in the $z$-field at glassy carbon occurs at a 59° angle of incidence. The lower reflectivity of glassy carbon also results in $x$- and $y$-components with much greater surface electric fields than at gold.

The last two materials, glass and silicon, are transparent at $2000\,\mathrm{cm}^{-1}$ ($k = 0$) but have different values for $n$. We see that silicon, with the larger $n$, is more reflective than glass; see equations (3.26) and (3.27). The maximum in the $z$-field occurs at a 58° angle of incidence for glass and 59.5° for silicon. In addition the relatively large values of the $x$- and $y$-components of the mean-square fields leads to a breakdown of the surface selection rule operative at metal surfaces. The variation of the mean-square electric fields as a function of distance from the surface will be examined in more detail next.

The plots of the mean-square electric field shown in Fig. 3.4 are diagnostic of the fields present at the interface between two media. As mentioned above, a standing-wave electric field is set up in the incident medium. Inspection of equations (3.35)–(3.37) shows that the period $p$ of the standing wave is given by

$$p = \frac{1}{2\bar{v}n_1 \cos\theta_1}. \tag{3.38}$$

Figure 3.5 is a plot of the relative mean-square electric fields as a function of distance from the same four reflecting media — gold, glassy carbon, glass, and silicon — examined in Fig. 3.4. The periodic nature of the mean-square electric fields in the incident medium is apparent. Also note that changing the angle of incidence from 78.5° for gold to 59° for glassy carbon results in a standing wave of shorter period via equation (3.38). We also see that for a highly reflective surface like gold, if the thickness of the phase-2 film is much less than the period of the standing wave, then the film will not interact with $s$-polarized light. Note also how the phase change occurring on reflection from glass has resulted in the $z$-field having a minimum at its surface. In the case of glass, and to a lesser extent silicon, the mean-square electric fields extend into the second phase and are constant because these two media are transparent and there is no interference from a reflected wave.
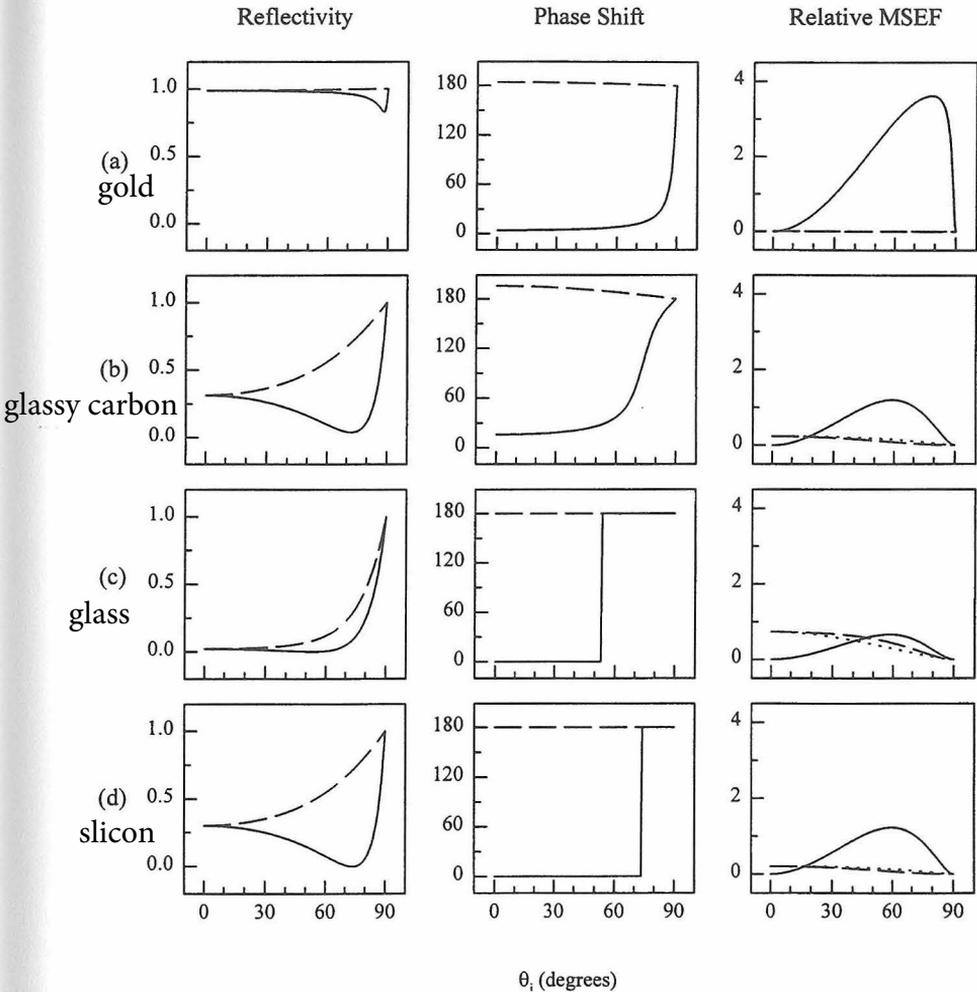
**Fig. 3.4** Reflectivity, phase shift, and relative mean-square electric fields at the surface of (a) gold, (b) glassy carbon, (c) glass, and (d) silicon as a function of the angle of incidence. The incident medium is air. For reflectivity and phase shift, values are shown for parallel (—) and perpendicular (– – –) polarization of the incoming light. The relative mean-square electric fields are shown for the $z$-(—), $x$-(----), and $y$-(– – –) components.

## Band Distortions

It has long been recognized that the experimentally determined band shapes of infrared reflection spectra of thin films can be shifted and distorted by the dispersion in the real part of the refractive index [10, 21]. However, a priori
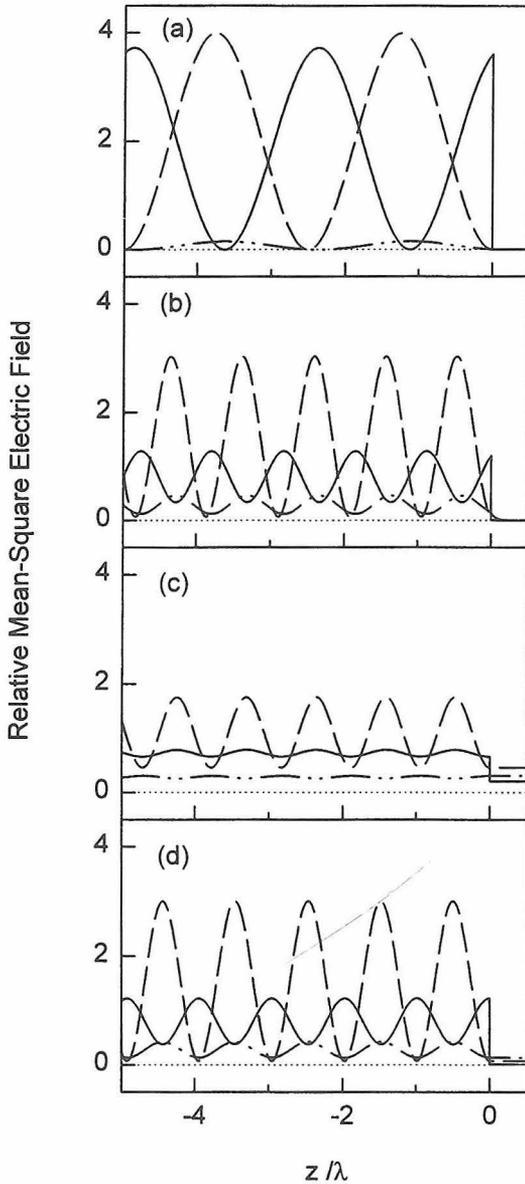
**Fig. 3.5** Relative mean-square electric fields in a 2-phase system as a function of distance from the interface. Phase 1 is air and phase 2 is (a) gold, (b) glassy carbon, (c) glass, and (d) silicon. The mean-square electric fields are shown for the $z$-(—), $y$-(– – –), and $x$-(– – – –) components. Distances have been normalized to the wavelength of the incident light, which corresponds to $2000\,\text{cm}^{-1}$.

predictions of band shapes are hindered by a complicated interplay of mean-square electric fields, angles of incidence, polarizations, and the reflectivities between different phases in a stratified medium. It is therefore valuable to examine a series of simulated spectra of absorbing films under differing conditions. As a starting point, Fig. 3.6 presents simulated data for $\hat{n}$ for a thin organic film. The absorption band has an absorption index $k(\bar{v})$ with a Gaussian line shape and a maximum value of 0.25 at $1730\,\text{cm}^{-1}$. These properties are similar to those for the carbonyl stretch of an ester functionality in a polymer like poly(methyl methacrylate). Using this $k(\bar{v})$, $n(\bar{v})$ can be calculated using the Kramers-Kronig relation given in equation (3.18). A plot of the resulting $n(\bar{v})$ is also shown in Fig. 3.6. It is seen that $n(\bar{v})$ has a derivative shape, decreasing on the high-energy side of the absorption band and increasing on the low-energy side.

The extent to which band shapes are dependent on angle of incidence is illustrated in Fig. 3.7. This figure shows a series of simulated spectra for a 1000-Å thick film, whose optical functions are as shown in Fig. 3.6, coated onto a glassy carbon substrate. To generate the spectra, the reflectivities for coated ($R$) and uncoated ($R_0$) substrates were calculated as a function of wavelength. The reflection analogue to absorbance is then given by $A = -\log(R/R_o)$. As is evident, the shapes of these spectra are reminiscent of that of $n(\bar{v})$, though the sign of the distortion changes in going from an angle of incidence of 20° to 80°.
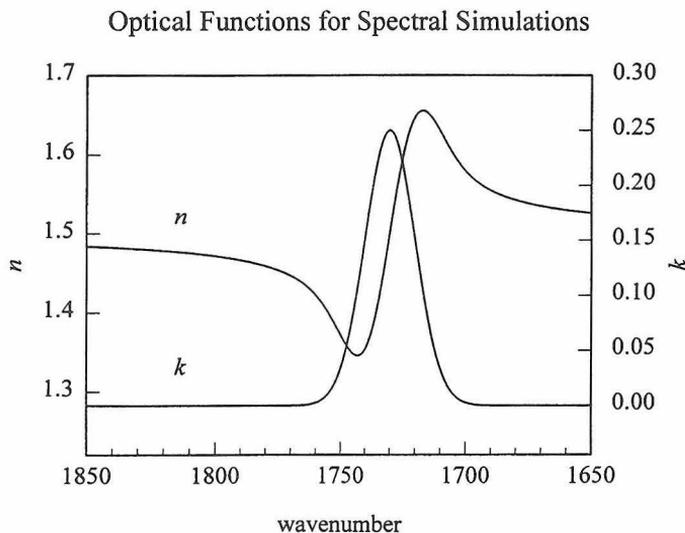
Optical Functions for Spectral Simulations



**Fig. 3.6** Absorption index $k$ and refractive index $n$ of a simulated infrared absorption band centered at $1730\,\text{cm}^{-1}$.
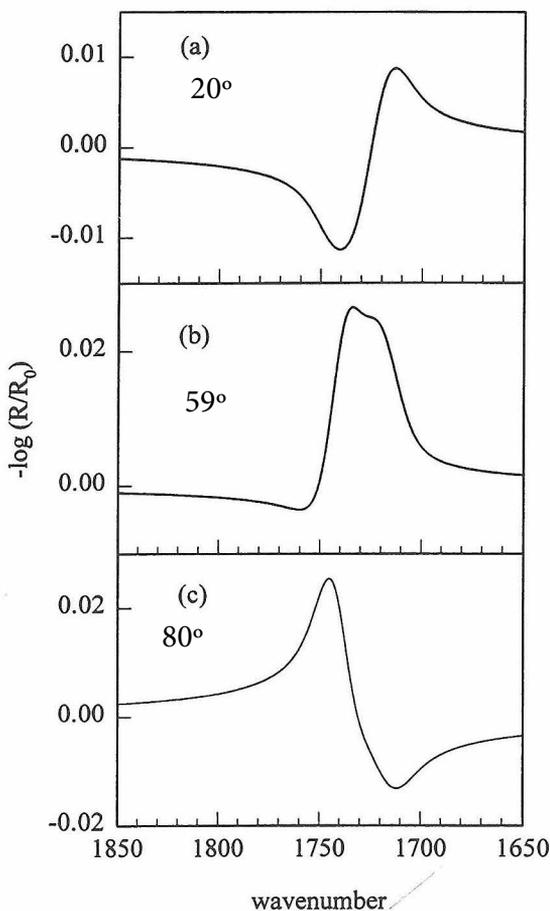
**Fig. 3.7** Simulations of a reflection absorption band of a 1000 Å-thick film whose optical functions are displayed in Figure 6. The incident medium is air and the substrate is glassy carbon whose optical functions are assumed to be constant ($n = 2.9$, $k = 1.3$) across the spectral region. This figure illustrates the changes that occur in the band profile as the angle of incidence of $p$-polarized light is changed from (a) 20°, to (b) 59° to (c) 80°.

To diagnose the role of $n(\bar{v})$ in determining these lineshapes, the calculations were repeated with a hypothetical film with $k(\bar{v})$ set to zero over all wavelengths, while the dependence of $n(\bar{v})$ in Fig. 3.6 was maintained. The results of these calculations are displayed in Fig. 3.8. Comparing these spectra with those in Fig. 3.7 reveals that at both high and low angles of incidence, the band shape is dominated by $n(\bar{v})$, whereas the spectrum at a 59° angle of incidence contains contributions from both $n(\bar{v})$ and $k(\bar{v})$.

Figure 3.9 shows the effect of varying the substrate on the band shapes and peak positions. As in Fig. 3.4, the substrates include gold, glassy carbon,
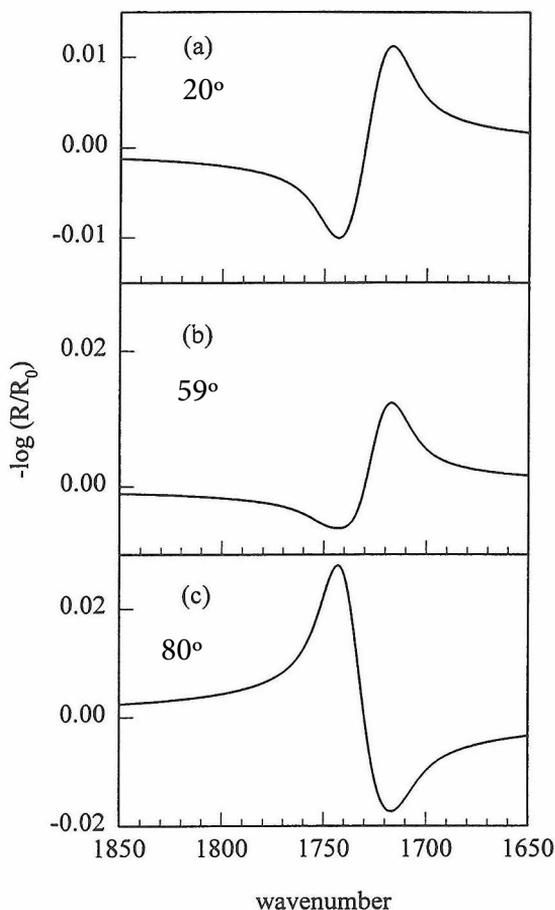
**Fig. 3.8** Spectral simulations under the same conditions as in Figure 7 except that the absorptivity of the film has been set to zero while retaining the same dispersion in *n*.

silicon, and glass. In all cases the angle of incidence was set at a value to produce the largest mean-square electric field at the surface of the substrate. Because of the convolution of optical effects, the distortion of the band shapes differ depending on the substrate. In some instances a maximum is observed at higher energies than the maximum for $k(\bar{v})$, and in some at lower energies. The following shows that these distortions are accurately predicted based on comparisons of observed and calculated spectra.

The distortions discussed above are evident in the spectra of poly(methyl methacrylate) (PMMA) films on glassy carbon. Figure 3.10 [22] shows both the observed and calculated spectra for three different PMMA film thicknesses (i.e., $3270 \pm 100$, $362 \pm 30$, and $78 \pm 15\,\text{Å}$) in the region of the
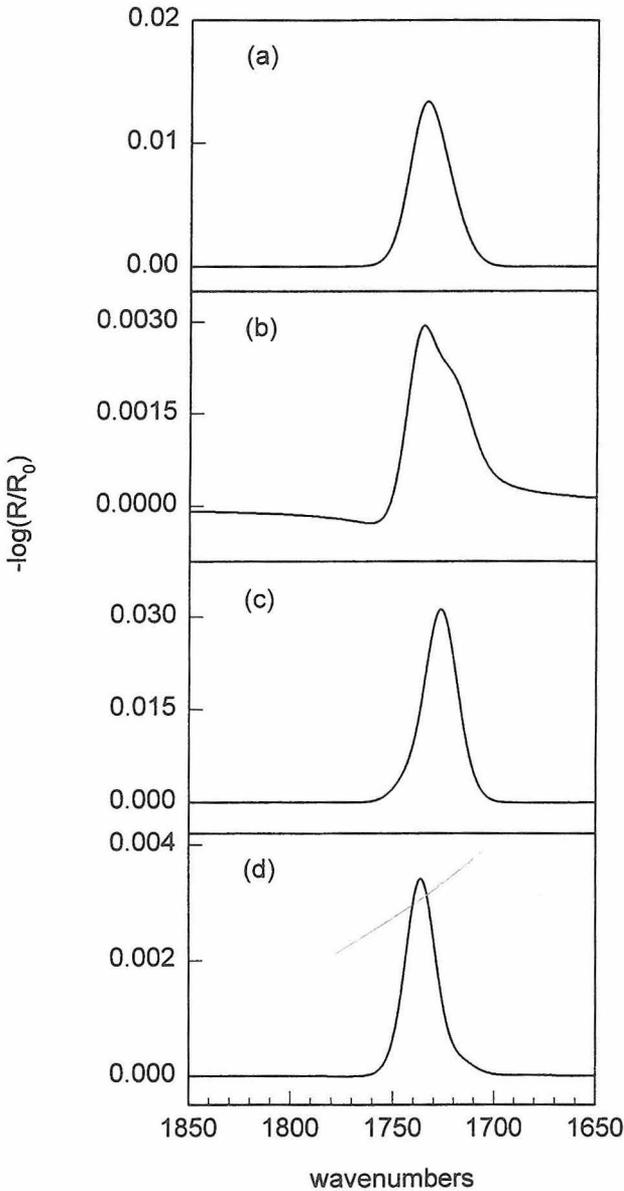
**Fig. 3.9** Simulated reflection spectra illustrating the effect of different substrates on band profiles. The spectra are for 100 Angstrom-thick films with optical constants given in Figure 6. The substrates and angle of incidence are: (a) gold, 70°; (b) glassy carbon, 59°; (c) glass, 58°; and (c) silicon, 59.5°. These angles are those that result in the largest relative mean-square electric field in the z-direction at the substrate interface.
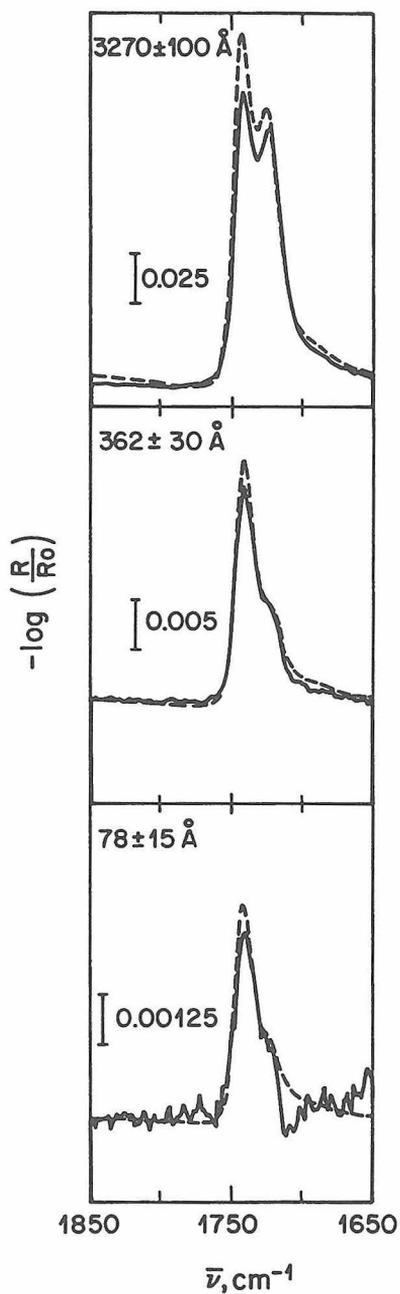
**Fig. 3.10** Experimental (—) and calculated (----) reflection spectra of the carbonyl stretching mode of poly(methyl methacrylate) films of various thicknesses on glassy carbon. The *p*-polarized light is incident at 60° (reproduced with permission from reference 22).

carbonyl stretching vibration obtained with $p$-polarized light incident at 60°. The calculated spectra were produced by starting with a transmission spectrum to generate an initial approximation for $k(\bar{\nu})$. This $k(\bar{\nu})$ was used to generate $n(\bar{\nu})$ through the Kramers-Kronig transformation. The resulting $k(\bar{\nu})$ and $n(\bar{\nu})$ data set was then used to calculate the transmission spectrum. Differences between the calculated and observed spectra were used to adjust $k(\bar{\nu})$, and the calculation cycle repeated until no further improvement in the fit was obtained. The final $k(\bar{\nu})$ and $n(\bar{\nu})$ data set was used to calculate the specular reflection spectrum at each film thickness. As discussed for the data in Fig. 3.8, optical effects can lead to large alterations in the shapes of reflection spectra compared to those found in transmission spectra. Furthermore these distortions are strongly dependent on film thickness as well as the polarization and angle of incidence of the incoming light. Figure 3.11 shows spectra of the same films as in Fig. 3.10 taken with a 20° angle of incidence. These alterations in peak location and shape, which are caused by the optical properties of the film, must be accounted for before assigning differences between reflection and transmission spectra to surface induced changes in the structure or chemical bonding of the film.

### Orientation Analysis

As was noted earlier, the anisotropy of the mean-square electric fields at highly reflective surfaces can be used to determine the spatial orientation of an organic film [23]. The analysis begins by recognizing that the magnitude of an infrared absorption is given by

$$A \propto |M \cdot E|^2, \tag{3.39}$$

where $M$ is the dipole moment derivative of the vibrational mode with respect to the normal coordinate of the vibration. Since maximum detection at a highly reflective surface occurs when $p$-polarized light is used at near-grazing angles of incidence, the electric field vector is oriented perpendicular to the surface (i.e., in the $z$-direction). It follows that the magnitude of the absorption will be given by

$$A \propto |M \cdot z|^2 \propto \cos^2 \theta, \tag{3.40}$$

where $\theta$ is the angle of orientation of the vibrational mode with respect to the surface normal. Thus the most strongly excited vibrations will be those with dipole transitions that are oriented perpendicular to the surface. This orientation dependence of the absorption intensity leads to observable differences between the spectra of isotropically and anisotropically oriented films, a situation that be exploited to deduce the orientation of molecules in
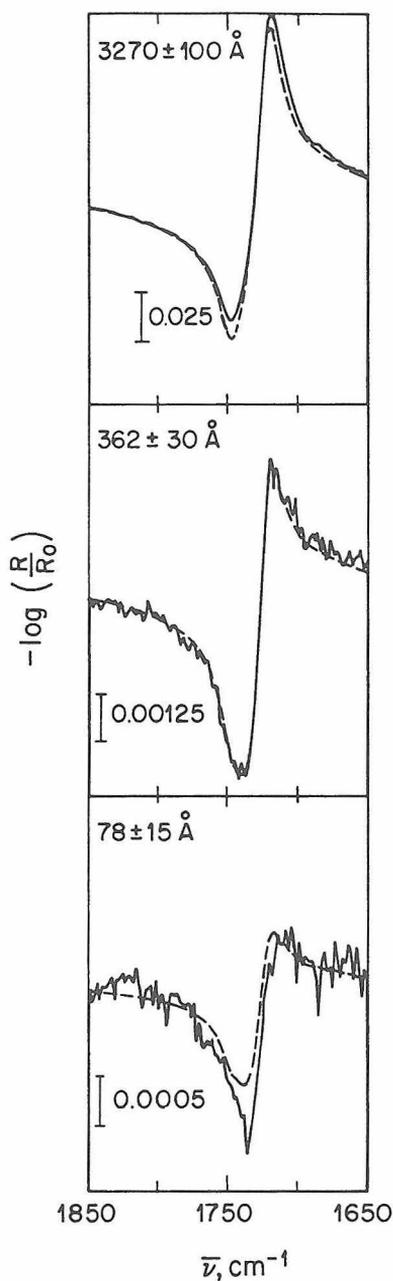
**Fig. 3.11** Experimental (—) and calculated (----) reflection spectra of the carbonyl stretching mode of poly(methyl methacrylate) films of various thicknesses on glassy carbon. The *p*-polarized light is incident at 20° (reproduced with permission from reference 22).

an ordered thin film. The average spatial orientation of a given vibrational mode can be calculated via

$$\cos^2 \theta = \frac{A_{\text{obs}}}{3A_{\text{calc}}},$$                    (3.41)

where $A_{\text{obs}}$ is the observed absorbance and $A_{\text{calc}}$ is the calculated absorbance for an isotropic film of equivalent thickness.

The above analysis has proved invaluable in the characterization of a variety of thin-film systems [1, 2, 3, 4, 5, 6]. There are, however, two important limitations that merit consideration. The first stems from the breakdown of the strong anisotropy of the electric fields that are present at surfaces with high reflectivities when using surfaces with low reflectivities. This situation, which was discussed earlier, results from the much larger presence of the $x$- and $y$-components of the electric fields at surfaces with low reflectivities (see Fig. 3.4). Thus the observed reflection spectrum for films coated on surfaces like glassy carbon contains contributions from a "mixed" surface electric field.

The second complication results from $\hat{n}$ being a tensor for an anisotropic medium. Most treatments do not consider $\hat{n}$ as a tensor but rather a scalar. Recently, however, an approach that treats the calculation of the reflection spectrum of a sample via a matrix transform method to account for the tensor quality of $\hat{n}$ had been developed [24]. The essence of the approach involves the iterative calculation of a reflection spectrum by varying the spatial orientation of the ordered film until reaching an optimal fit with the experimental spectrum. This approach represents an important refinement of orientation determinations, as will be demonstrated for one example in the next section. It is nevertheless important to note that use of all orientational analyses are only valid if the vibrational modes of the adsorbate are not strongly perturbed as a consequence of immobilization.

## 3.3  EXPERIMENTAL CONSIDERATIONS

IRS has long been an important method for the investigation of structure and bonding in organic materials. The extension of this technique to the investigation of the structure of thin films as surface coatings has generally been limited by the ability of infrared instrumentation to detect small amounts of material on a surface. Recent instrumental developments, such as advances in Fourier transform infrared (FT-IR) technology, make such characterization much more tractable.

Given the small amounts of material present in most thin films and the resulting low magnitude of their spectra, one of the limiting factors in the application of IRS to specular reflectance has been the attainment of the requisite signal-to-noise (S/N) ratio sufficient to provide tractable spectra. For instance, in the case of spontaneously adsorbed monolayers, absorbances are generally on the order of $10^{-4}$ or less, requiring a S/N ratio often unattainable without specialized detectors. Recent improvements in detector design and electronics have led to high-quality, "off the shelf" detectors that provide more than adequate S/N for most experiments.

The advent of computer technology has also been valuable to the development of reflectance methods in FT-IR spectroscopy. Improvements in computer design have allowed the replacement of vendor-built minicomputer systems with commercially available systems as well as a notable decrease in the calculation time required for the Fourier transformation analysis.

The general experimental design for external reflectance infrared spectroscopy varies only slightly from experiment to experiment. In its most basic form, the experiment requires four components. These include a stable source of broadband infrared radiation, a method for mounting the sample in the infrared beam, a method for separating the incident light into its component polarizations, and a detector, all of which are coordinated through a computer-driven data acquisition and control system. By far the most common instrumental arrangement utilizes Fourier transform technology by combining a Globar type blackbody emission source, Michelson interferometer, and liquid-nitrogen-cooled HgCdTe or InSb detector. Commercial versions of these instruments are now capable of providing the stability and low noise levels necessary for reflectance experiments at submonolayer levels. This being true, judicious choice of components is still a necessity in the construction of such an instrument.

The selection of an appropriate IR source has become much less problematic in recent years. The development of Globar sources, which function as stable blackbody generators, has reached the point where stability is not a major concern. A remaining consideration currently involves the external cooling method for the source. Recently ceramic technology has allowed the more combersome liquid-cooling methods to be replaced by much simpler air-cooled sources that provide stable outputs over a fairly long lifetime.

Coincident with the progress in computer technology has been a general increase in the availability of high-performance detectors. For most applications, a liquid-nitrogen-cooled HgCdTe broad- or narrowband detector provides the requisite low noise levels.

The convoluted dependence of specular reflection spectra on polarization, angle of incidence, and substrate optical properties is a challenging problem

for potential users of the technique. Insights into the physical optics of the measurement must be developed in order to optimize sampling configuration. Moreover these complications must be accounted for when using the spectra obtained in this mode for quantitative measurements or for structural interpretations based on peak positions and band shapes. For example, the nature of the standing wave electric field near the substrate surface results in a nonlinear dependence of absorption on film thickness.

There are several sampling approaches for specular reflectance measurements; all are designed to maximize detection capabilities while minimizing contributions from background interference. The vast majority of specular reflectance experiments involves the characterization of thin organic films deposited onto metallic (i.e., highly reflective) substrates. As was discussed in the last section, the experimental configuration for maximum detectability has an incoming *p*-polarized beam at grazing angles of incidence. Using this configuration with high-performance instrumentation, it is possible to characterize submonolayer quantities of an adsorbate. Orientational information can also be derived from such spectra via the infrared surface selection rule [10, 16].

External reflection spectra can be measured in several ways with commercially available, fixed or variable angle accessories that readily can be mounted into the sample compartment of an FT-IR spectrometer. In Fig. 3.12, the optical layout of the Versatile Reflection Attachment (VRA, Harrick Scientific Corp.) is shown. This accessory allows the angle of incidence to be varied continuously from 15° to 85° without realignment. This is accomplished by rotation of the sample-mirror combination, which has a fixed angle of approximately 100° between them, about an axis that lies along the intersection of the sample and mirror planes. This accessory can accommodate a range of sample sizes and is convenient for examining thin films supported on a smooth metal substrate, such as gold or silver, vapor deposited on a microscope slide. While the optimum angle of incidence for characterizing films on gold in the mid-infrared region of the spectrum is 88°, it is often advantageous to use a lower incidence angle because a circular IR beam incident at 88° is elongated to nearly 30 times over its original diameter. Thus, unless very large samples or small beam diameters are used, much of the light will not impinge on the sample. In contrast, an 80° angle of incidence spreads the beam by only a factor of six, simplifying the measurement. Larger samples, such as computer disks, are more easily handled if mounted horizontally. Accessories optimized for such purposes have been developed. However, changing the angle of incidence is not as convenient as with the VRA, and most accessories are set up to provide a fixed angle of incidence.

The spreading of the IR beam across the sample at high angles of incidence limits the spatial resolution of the technique. Importantly, acces-
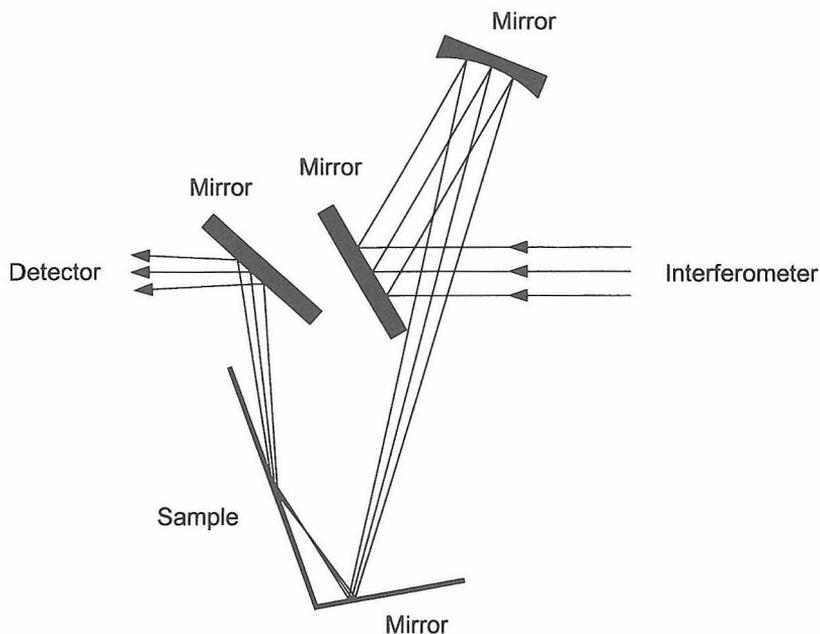
**Fig. 3.12** Optical layout of an FT-IR spectrometer accessory for performing specular reflection measurements.

sories are available for use with an infrared microscope [25] that allow measurements to be made at grazing angles of incident with a spatial resolution of $\sim 50\,\mu$.

A more challenging problem involves the analysis of films deposited on nonmetallic substrates, such as silicon or carbon surfaces. Maximum detectability in these cases occurs at an incident angle of $\sim 70°$ with respect to the surface normal. In comparison to characterizations at highly reflective surfaces, those at surfaces with low reflectivities suffer from two complications. The first is the accentuation of the distortion of spectral band shapes that results from the dispersion in the refractive index of the film in the vicinity of absorption features (see Section 3.2). The second is the "breakdown" in the surface effect that gives rise to the surface selection rule at metallic surfaces (see Section 3.2). Both complications arise from the lower reflectivity of substrates like silicon and carbon.

Perhaps most important in reflectance measurements at substrates coated with thin films is the choice of a material for a reference spectrum. The most common reference is an uncoated sample substrate that has been cleaned using acidic or organic solvents immediately prior to use. These "bare"

references are sufficient for use with samples having large absorbances but can be troublesome for samples with low signal strengths (i.e., ultrathin films). Contaminants on reference substrates have serious consequences in such cases by introducing artifacts into the resulting spectrum. To counteract these effects, reference samples are often prepared by use of a protective film that minimizes adventitious contaminant adsorption and does not have spectral features that overlap with those of the sample film. Examples of such films include perdeuterated [26] or fluorinated [27] organothiolates adsorbed at gold. Both materials have low surface tensions and are thereby not highly susceptible to contaminant adorption. However, where perdeuterated thiolates are of use over a significant portion of the mid-IR spectral region, the fluorinated organothiolates have strong spectral features associated with C–F stretching modes that limit their usefulness largely to the C–H stretching region.

Another critical consideration in the design of infrared specular reflectance characterizations involves an understanding of the environmental requirements for a particular experiment. A significant source of interference in low signal measurements is the strong absorbance of water vapor and carbon dioxide in critical regions of the infrared spectrum. At the typically small absorbance levels for thin films, inadequate removal of these interferences can result in a considerable masking of spectral details. Masking by water vapor can be especially problematic because of the overlap of its envelopes of stretching and bending modes with the C–H and C=O stretching regions. The use of vacuum techniques has been quite successful in dealing with this interference, but is available on only a few commercial instruments. Moreover the direct translation of the results of *in vacuo* characterizations to actual *in situ* conditions may prove problematic.

A more common method for dealing with water vapor and carbon dioxide is through the use of efficient and consistent purge methods combined with spectral subtraction techniques to remove signals from ineffectively compensated interferences. Instrument designs currently contain the requisite "plumbing" to purge efficiently the spectrometer with either dry air or nitrogen. Purging the bench, for example, with a clean, dry purge gas (e.g., boil-off from liquid nitrogen) can diminish water interference to a level where the resulting spectroscopic features are negligible compared to those of the sample. Spectral subtraction with the necessary reference spectrum can then be used to compensate for any residual interference signal, resulting in a high-quality sample spectrum.

Another approach for discrimination against the "background" signals of the surrounding media employs polarization modulation (PM) techniques [28]. These techniques take advantage of the anisotropy of the mean-square electric field near a highly reflective surface for *p*- versus *s*-polarized incident light. Because only the *z*-component of the electric field is present near the

surface, immobilized films absorb only $p$-polarized light. The surrounding, isotropic medium, however, absorbs both $p$- and $s$-polarized light.

In PM experiments the polarization of the infrared light is modulated at kilohertz frequencies between the two polarization states through the use of a photoelastic modulator in conjunction with a polarizer. A photoelastic modulator is an IR transparent crystal with an isotropic refractive index when unstressed. The application of a resonant periodic strain along one axis of the crystal with a piezoelectric actuator induces an anisotropy in the refractive index of the crystal, which results in a phase retardation and hence, a rotation of the polarization of the incident beam. The addition of a fixed polarizer to the optical path that is aligned to pass either $s$- or $p$-polarized light completes the setup, with the beam impinging on a surface modulated between the two polarization states. The signal from the reflection experiment is then demodulated using phase-sensitive detection to generate a difference spectrum $(I_p - I_s)$ between the $p$- and $s$-polarized components of the signal. The differential reflectance spectrum $(S)$ of the sample is obtained as the ratio of the difference spectrum to the sum $(I_p + I_s)$:

$$S = \frac{(I_p - I_s)}{(I_p + I_s)}. \tag{3.42}$$

A block diagram of this instrumentation is shown in Fig. 3.13. Further details of the basic principles of this technique, which has also been successfully applied to compensate for the background of *in situ* electrochemical studies [5, 29, 30], as well as recent experimental advances are available [31, 32].
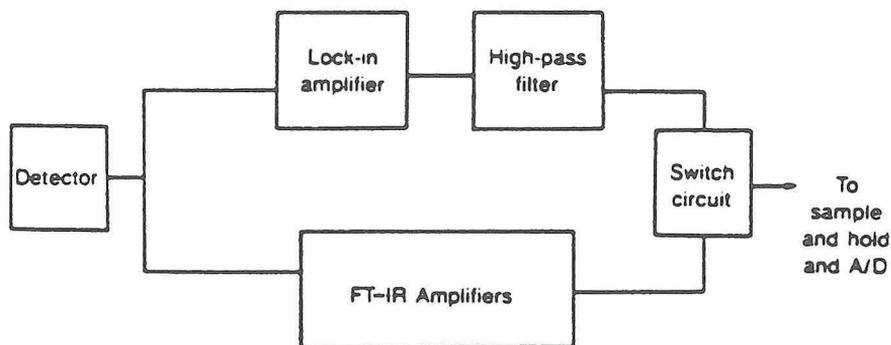


**Fig. 3.13** Schematic of a signal processing arrangement for a polarization modulation measurement. The signal for the detector amplifier is split into two channels, with each channel demodulated separately (reprinted with permission from reference 5).

## 3.4  APPLICATIONS

The previous discussions lay a foundation for the application of IRS to a wide range of surface characterizations. Applications have ranged from the identification of the products from a plasma-induced modification of the surface of a polymeric film [33]; the determination of the average spatial orientation of ordered organic films at metal [23, 34, 35, 36, 37, 38, 39, 40, 41], carbon [24], and aqueous [41, 42] interfaces; the delineation of the effects of applied potential on the composition of a redox-transformable organic adsorbate at electrode surfaces [43, 44, 45]; to the reactions of gas phase species at surfaces under ultrahigh vacuum [46]. In view of the breadth of these applications, the following discussion is limited to three types of characterization problems. The first example deals with the structural characterization of organized organic thin films. This example illustrates the use of IRS as a probe of the spatial orientation of monolayer and multilayer films. The second example deals with the dependence of the composition and structure of an organic monolayer films with a pendent redox-transformable functionality. This example demonstrates the capability of IRS as an *in situ* structural probe of liquid-solid interfaces. The third example describes a study of the composition of thin films of aluminum nitride. This example shows the utility of IRS as a probe of the effects of preparation and handling on the composition of this material important to microelectronics research.

### Organized Thin Films

In selecting representative applications of IRS characterizations of samples in a specular mode, we first discuss the results of a series of characterizations of organized monolayer and multilayer films of organic compounds. These examples demonstrate the strengths of this characterization approach by unraveling details concerning both the composition and average spatial arrangement of the thin film. The first example examines the composition and spatial orientation of the monolayer formed by the spontaneous adsorption of a long alkyl chain length alkanoic acid (i.e., arachidic acid, $CH_3(CH_2)_{18}COOH$) at ambient silver surfaces [47]. The interest in such systems stems from the high relative degree of order of the organic structures which are formed by this and other adsorbate-substrate combinations (e.g., organosulfur compounds at gold surfaces [48,49]) in comparison to the morphological and compositional heterogeneity of functionalized polymer surfaces. This attribute, coupled with ease of preparation, has lead to an explosive growth in the use of these systems as models for examining the structural origins of a host of interfacial phenomena (e.g., electron transfer, wettability, lubrication, and biocompatibility) [49] and as platforms for the construction of chemical sensors and other forms of analytical transduction schemes [48].

Figure 3.14 gives details about both the mode of interaction between arachidic acid and the ambient silver surface and the packing density of the alkyl chains. The presence of the strong band at $1400\,cm^{-1}$ and the weak, barely detectable band at $1514\,cm^{-1}$, coupled with the absence of a band around $1730\,cm^{-1}$, reveals that the chemisorption of the carboxylic acid group and the thin layer of silver oxide present at ambient silver surfaces transforms the acid to a carboxylate salt. A dispersion of the arachidic acid in KBr has an absorption band near $1730\,cm^{-1}$, which is the $\nu(C{=}O)$ mode for a protonated carboxylic acid. As judged by comparison to spectra for silver carboxylate salts, the bands at $\sim 1514$ and $1400\,cm^{-1}$ are assigned to the $\nu_a(COO^-)$ and $\nu_s(COO^-)$ modes, respectively. Importantly, the much larger absorbance of the $\nu_s(COO^-)$ mode with respect to the $\nu_a(COO^-)$ mode argues that the carboxylate group is symmetrically bound as a bridging ligand to the silver surface, an assertion consistent with the peak positions for bulk metal carboxylate salts of bridging ligands.

The monolayer spectrum in Fig. 3.14 also contains information that serves as a basis for the development of a conformational description of the alkyl chains. Earlier studies of crystalline hydrocarbons [50, 51], which were undertaken in part to aid in the characterization of the chain structure of the bilayer structure of cell membranes, have found that the coupling of the $\omega(CH_2)$ and $\gamma(CH_2)$ modes is a signature of alkyl chains composed of all-trans conformational sequences. Thus the envelope of the $\omega(CH_2)$ and
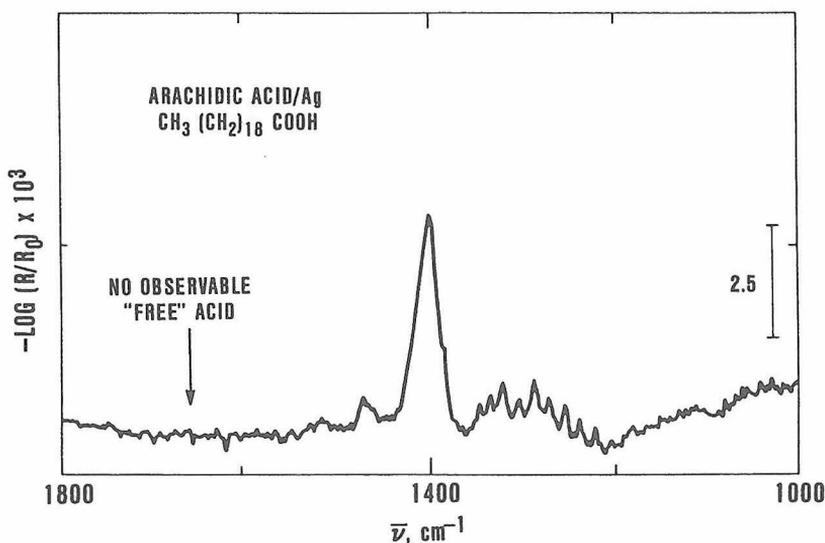


**Fig. 3.14** Infrared specular reflectance spectrum between 1800 and $1000\,cm^{-1}$ for a spontaneously adsorbed monolayer from aracidic acid at silver (adapted with permission from reference 47).

$\gamma(CH_2)$ between 1350 and 1200 cm$^{-1}$ is diagnostic of an extended chain conformation. Though unclear as to the extent of conformational defects, it follows that the resulting interfacial structure exists in a densely packed environment.

Further insight into the structure of the alkyl chains of the monolayer formed from arachidic acid can be gleaned from the spectrum in Fig 3.15. This figure presents both an experimental and calculated spectrum in the C–H stretching region. The bands at 2917 and 2851 cm$^{-1}$ are assigned to the $\nu_a(CH_2)$ and $\nu_s(CH_2)$ modes, respectively. Bands attributed to the methyl modes are also evident, with the in-plane $\nu_a(CH_3)$ mode at 2965 cm$^{-1}$ and two bands for the Fermi-resonance couplet of the $\nu_s(CH_3)$ mode at 2938 and 2879 cm$^{-1}$. Importantly, the positions of the methylene stretching modes are indicative of a densely packed array of alkyl chains, which is consistent with the presence of the envelope of the $\omega(CH_2)$ and $\gamma(CH_2)$ modes in Fig. 3.14.

Details about the spatial orientation of the alkyl chains can be quantitated by an examination of the absorbances of the methylene modes for the calculated and experimental spectra. In this case both the average tilt ($\theta$) and twist ($\phi$) of the alkyl chains (see Fig. 3.16) can be determined by
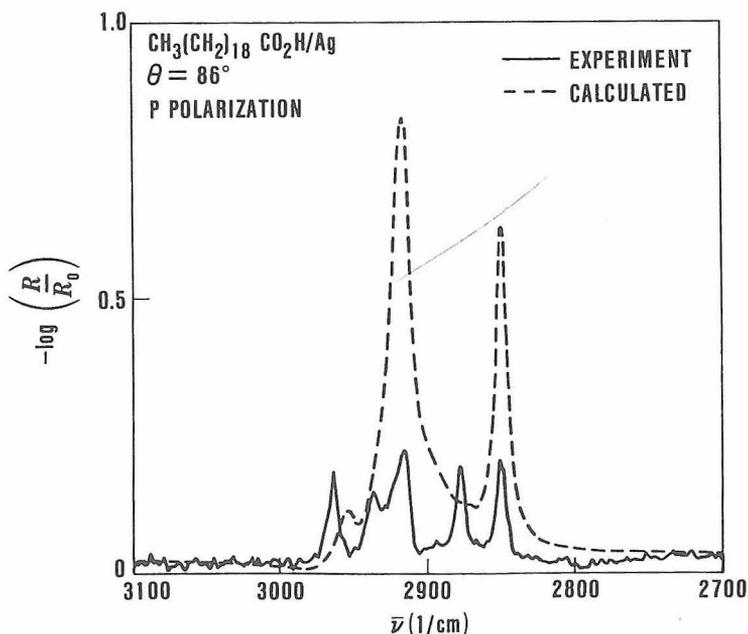


**Fig. 3.15** Observed (—) and calculated (-----) infrared specular reflectance spectrum between 3100 and 2700 cm$^{-1}$ for a spontaneously adsorbed monolayer from aracidic acid at silver (adapted with permission from reference 47).
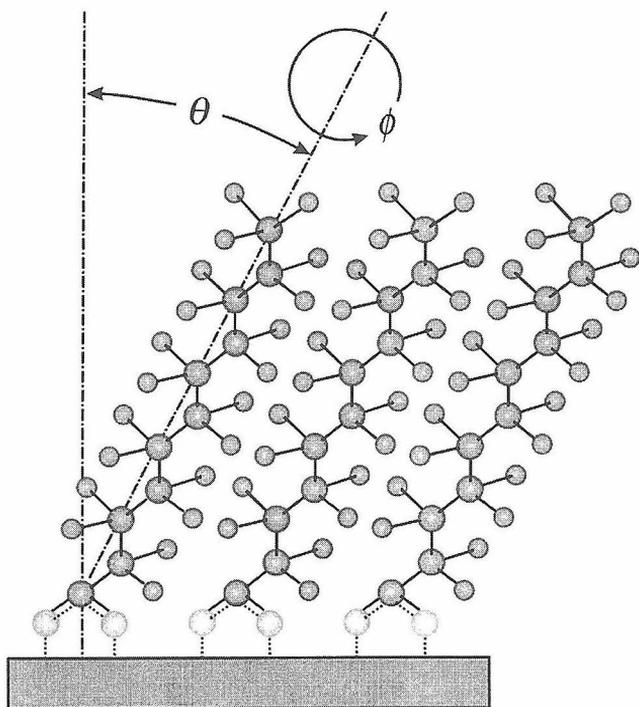
**Fig. 3.16**  Definition of the tilt angle $\theta$ and twist angle $\phi$ of an all-trans alkyl chain with respect to a planar surface.

recognizing that the transition dipoles for the $\nu_a(CH_2)$ and $\nu_s(CH_2)$ modes are orthogonal to each other as well as to the molecular axis of an extended alkyl chain. For such a system, equation (3.41) can be recast as

$$\sin^2 \theta \, \cos^2 \phi = \frac{A_{obs}^{\nu_s}}{3A_{calc}^{\nu_s}}. \tag{3.43}$$

$$\sin^2 \theta \, \cos^2 \phi = \frac{A_{obs}^{\nu_a}}{3A_{calc}^{\nu_a}}. \tag{3.44}$$

This treatment yields an average value for $\theta$ of 24° and of 48° for $\phi$. These angles are consistent with a carboxylate head group bound to silver as a symmetric bridging ligand. That is, a $\theta$ of 24° follows from the expectation of a fully extended chain conformation connected to a symmetrically bound carboxylate group.

An analysis of the chain structure for organized thin films supported on surfaces with low reflectivity can be performed as well. An example of such

a situation is presented in Fig. 3.17 [1]. This figure shows an observed and calculated spectrum in the C–H stretching region for a five-monolayer Langmuir-Blodgett film of cadmium arachidate supported on a glassy carbon substrate. Based on the low reflectivity of the support, the optimal angle of incidence for detection is at a much lower value than at a metal substrate (see Fig. 3.5). The derivative-shape of the spectra arises from the importance of the reflectivity at the air-film interface along with the order of the chain structure. For this multilayer system the comparison of the observed and calculated spectrum, where the calculated spectrum was obtained by the iterative process briefly described in Section 3.2, yields an average $\theta$ of 15° and an average $\phi$ of 45°.

### Redox Transformations at Electrochemical Interfaces

In contrast to the above example, the application of IRS to probe processes at electrochemical interfaces has two major obstacles. The first is the strong absorption of the electrolytic solution. The second is the discrimination of very small absorbance changes (i.e., absorbances of $10^{-5}$–$10^{-4}$) in the presence of the large (and sometimes overwhelming) background absorbance of the electrolytic solution. A solution to the first obstacle is the use of
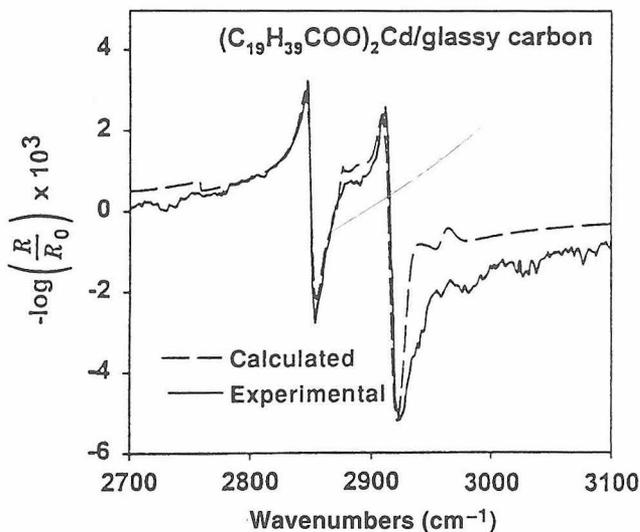


**Fig. 3.17** Observed (—) and calculated (-----) infrared specular reflectance spectrum between 3100 and 2700 cm$^{-1}$ for a five-monolayer Langmuir-Boldgett film of cadmium arachidate on a glassy carbon substrate. The *p*-polarized light is incident at 55° (adapted with permission from reference 1).

an electrochemical cell in which the contacting solution layer is held at thicknesses of a few microns for aqueous electrolytes and tens of microns for some nonaqueous media [29, 30]. Solutions to the second obstacle often employ electrochemical [29, 30] or optical (e.g., polarization; see Section 3.3) modulation schemes that are coupled with phase-sensitive detection techniques.

Figures 3.18 and 3.19 give an example of the design and optical layout of a thin layer cell. Such cells are designed for operation primarily in a specular reflection mode with the incoming beam impinging on an IR-transparent hemispherical window, passing through the thin layer of electrolytic solution, and reflecting off the electrode. The use of a hemispherical window ensures that light reflected from the air-window interface does not impinge on the detector. This design, coupled with the "beam-steering" peripheral mirrors in Fig. 3.19, facilitates optimization of the angle of incidence at the solution-electrode interface, which is a strong function of the optical properties of both the window material and electrolytic solution.
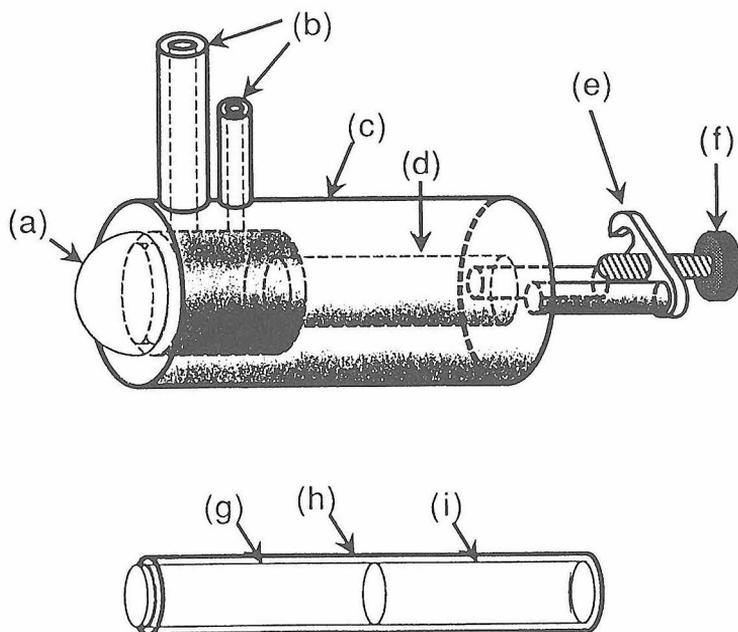


**Fig. 3.18** Schematic diagram of a thin-layer spectroelectrochemical cell for characterization of organic coating at electrode surfaces by infrared specular reflectance spectroscopy. Top: (a) hemispherical window (retaining window bracket not shown); (b) solution inlet and outlet ports, (c) Kel-F cell body, (d) barrel, (e) plunger retaining screw, and (f) retaining screw. Bottom: (g) borosilicate glass core, (h) Kel-F jacket, and (i) brass core (reproduced with permission from reference 42).
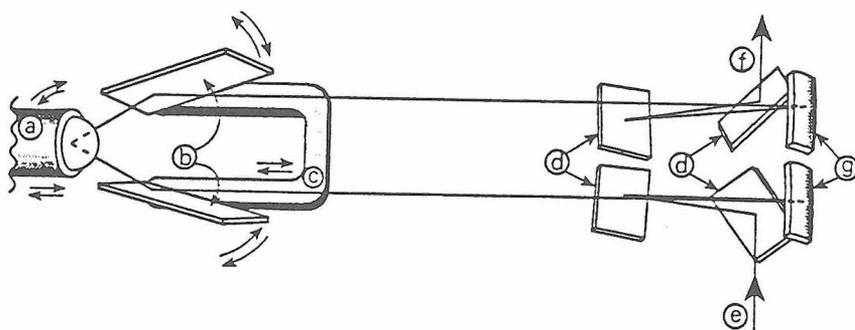
**Fig. 3.19** Illustration of an optical layout for an *in situ* spectroelectrochemical characterization by specular reflectance spectroscopy. The cell assembly (a–c) and the focus projection accessory (d–f) are designed to provide flexibility to select the optimal irradiation geometry as dictated by the optical properties of the experimental components. Left: (a) front of cell (see Figure 18), (b) peripheral mirrors, and (c) arm of peripheral mirrors (which translates parallel to the optical axis). Right: (d) plane mirrors, (e) incoming beam from spectrometer, (f) outgoing beam to detector, and (g) concave mirrors to project focal plane (reproduced with permission from reference 42).

The unique structural features of spontaneously adsorbed monolayers from organosulfur compounds has also attracted the imagination of the electrochemical community [9, 49]. These systems have opened new avenues for explorations of heterogeneous electron-transfer mechanisms, electrical double-layer theories, and the creation of new types of electrochemical-based sensors [9, 49]. In each of the above cases, it is important to determine if the electrochemical transformation of a pendent redox moiety induces a structural change in the monolayer. For example, redox transformations may cause reversible/irreversible changes in the structure of the underlying polymethylene chain and/or in the double-layer structure at the interface formed by the solution-monolayer contact.

Figures 3.20 through 3.24 present the results of a study that examines the affects of a redox transformation on the structure of an organic monolayer film [43]. These results are for a monolayer prepared by the chemisorption of 11-mercaptoundecyl ferrocenecarboxylate $[(\eta^5 - C_5H_5)Fe(\eta^5 - C_5H_4)-COO(CH_2)_{11}SH$ (abbrev. $FcC_{11}SH$), where Fc denotes the ferrocenyl group] at a gold electrode. Figure 3.20 shows a set of cyclic voltammetric current-potential $(i - E)$ curves for the as-formed monolayer. The wave observed as the applied voltage is scanned from $+0.20$ to $+0.85$ V reflects formally the oxidation of the Fe(II) of the ferrocenyl moiety to Fe(III), whereas the wave found upon the change in scan direction arises from the reduction Fe(III) to Fe(II). Both the shapes of the $i - E$ curves and the linear dependence of peak currents with scan rate are consistent with the
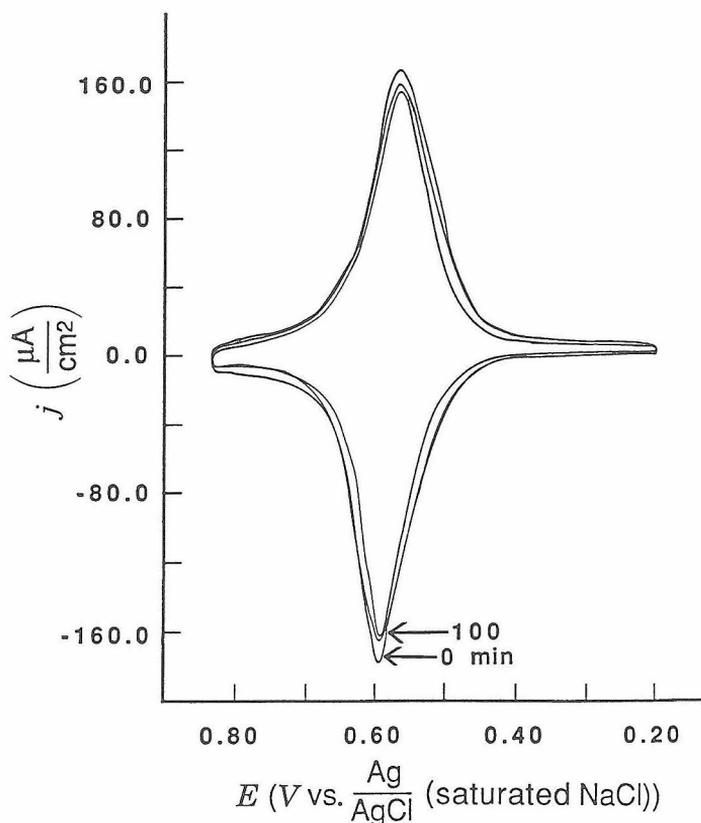
**Fig. 3.20** Cyclic voltammetric curves for a monolayer formed from $FcC_{11}SH$ at gold. The scan rate is $400\,mV/s$, with each scan recorded after holding the applied voltage at $+0.20\,V$ for the noted time period (adapted with permission from reference 43).

electrolysis of an immobilized redox species [9]. The general repeatability of the $i - E$ curves demonstrates the electrochemical stability of the immobilized species.

The electrochemical data provide two additional insights into the structure of the $FcC_{11}SH$-based monolayer. First, the charge passed to electrolyze the ferrocenyl moiety can be used to determine the surface concentration of the monolayer. Based on such an analysis, the surface coverage corresponds to a packing density limited largely by the size of the ferrocenyl end group. Second, the charging current that flows before and after oxidation of the ferrocenyl group changes markedly. This change reflects one of two (or a combination of both) possibilities. One possibility is a change in the capacitance of the interfacial structure that arises from the
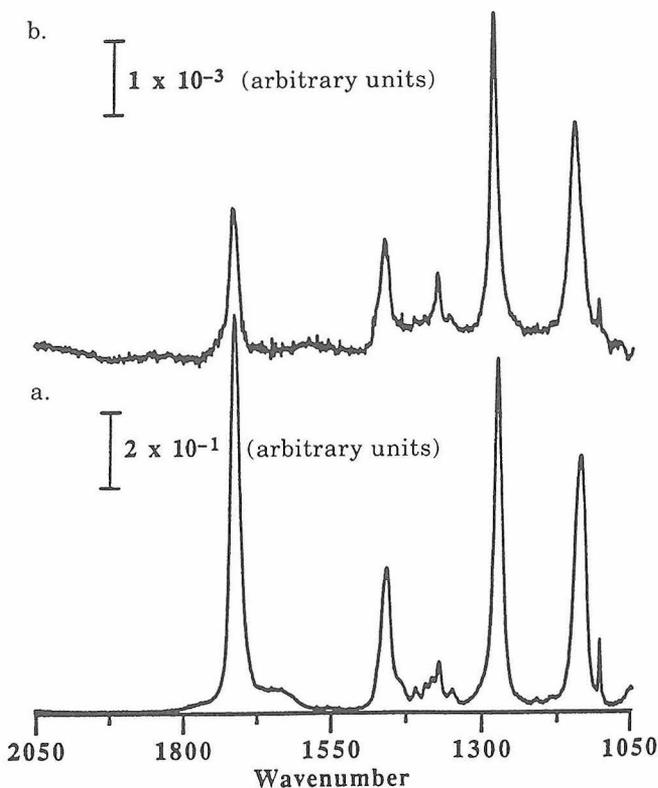
**Fig. 3.21** Infrared specular reflectance spectrum between 2050 and 1050 cm$^{-1}$ of (a) a KBr pellet of FcC$_{11}$SH and (b) of a spontaneously adsorbed monolayer from FcC$_{11}$SH at gold. The monolayer spectrum was collected at an incident angle of 82° using *p*-polarized light (adapted with permission from reference 43).

creation of a cationic ferrocenyl group; the other is a change in the structure of the monolayer because of the repulsion of closely spaced, charged end groups. Gaining insight into the viability and relative importance of both possibilities is critical to the interpretation of data from studies aimed at the use of this system as a model interfacial system.

Figures 3.21 and 3.22 presents the IRS spectrum for a monolayer from FcC$_{11}$SH at gold. The former is the spectrum in the low-energy region, and the latter in the high-energy region. Both figures include spectra for the precursor dispersed in a KBr pellet. Bands diagnostic of the pendant group on the monolayer include the carbonyl stretching modes at 1714 cm$^{-1}$, the two C–O stretching modes at 1147 and 1283 cm$^{-1}$, the ferrocene ring C–H stretching modes at ~3100 cm$^{-1}$, and the ferrocene ring modes between
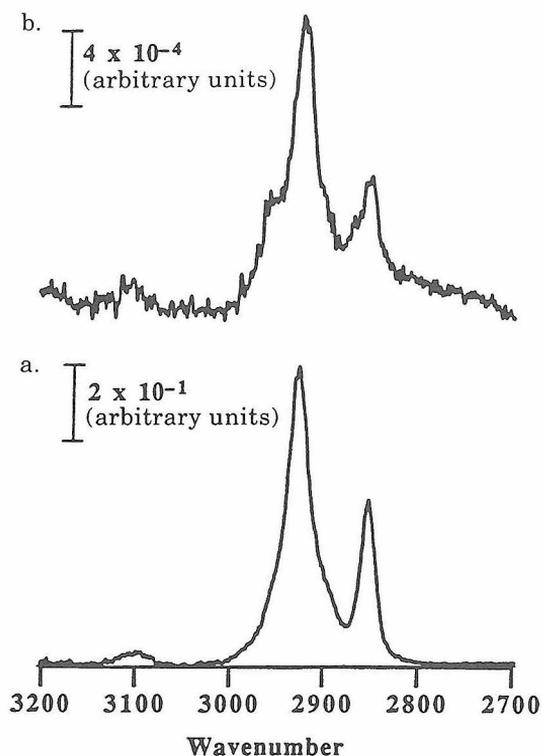
**Fig. 3.22** Infrared specular reflectance spectrum between 3200 and 2700 cm$^{-1}$ of (a) a KBr pellet of FcC$_{11}$SH and (b) of a spontaneously adsorbed monolayer from FcC$_{11}$SH at gold. The monolayer spectrum was collected at an incident angle of 82° using *p*-polarized light (adapted with permission from reference 43).

1445 and 1350 cm$^{-1}$. The presence of these modes, along with the methylene asymmetric and symmetric stretching modes between 2950 and 2800 cm$^{-1}$, confirms the formation of the FcC$_{11}$SH monolayer.

A series of potential modulation spectra is shown in Figs. 3.23 and 3.24 for a monolayer from FcC$_{11}$SH at gold in 1.0 M HClO$_4$(aq). In this mode a reflectance spectrum ($R_0(\bar{v})$) was first scanned at a base voltage of $+0.20$ V (vs. Ag/AgCl (saturated KCl)). The applied voltage was then stepped to a selected value at which another spectrum ($R(\bar{v})$) was scanned. The two single-beam spectra are then combined to yield a differential spectrum ($-\log(R(\bar{v})/R_0(\bar{v}))$). Several notable changes in the spectra are evident as the applied voltage becomes increasingly positive. The most notable changes in Fig. 3.23 are for the vibrational modes associated with the ester linkage between the ferrocenyl group and the polymethylene chains. Of the bands
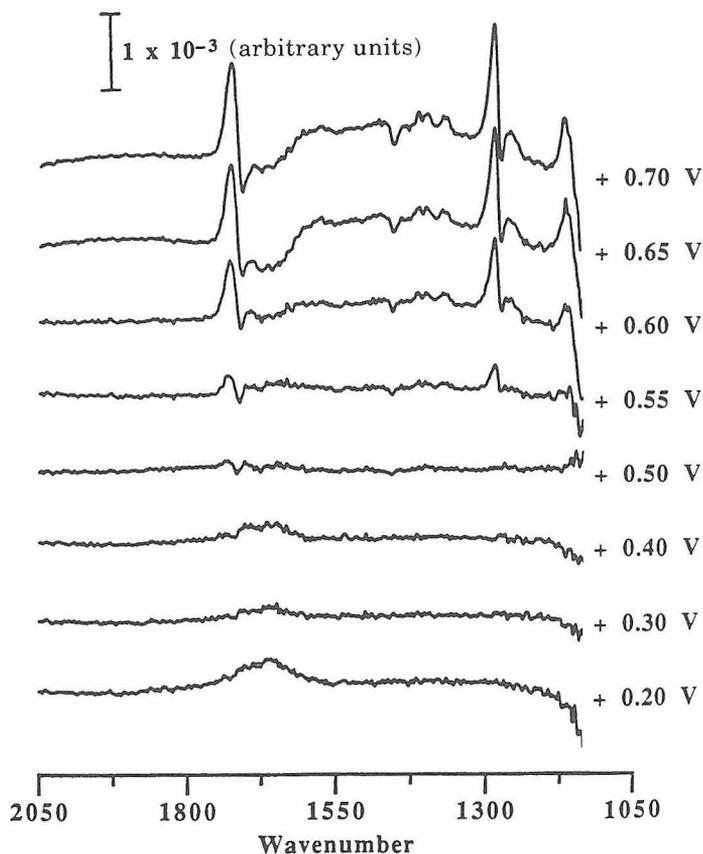
**Fig. 3.23** *In situ* differential spectra of a monolayer from $FeC_{11}SH$ at gold in 1.0 M $HClO_4$ between 2050 and 1050 $cm^{-1}$ as a function of applied voltage. The reference spectrum was taken at $\pm 0.20$ V (reproduced with permission from reference 43).

not obscured by features of the supporting electrolyte (i.e., the overlap of the C–O of the ferrocenyl group and the Cl–O mode of the supporting electrolyte at $\sim 1140$ $cm^{-1}$), derivative-shaped spectral features are observed. The shapes result from the shift of the positions of these vibrational modes to higher energy that results from the oxidation of the ferrocenyl group.

Changes in the high-energy region of the spectrum (Fig. 3.24) are also evident as a consequence of the oxidation of the ferrocenyl moiety. Six bands appear as the applied voltage becomes more positive. Importantly, the bands at 2929, 2872, and 2858 $cm^{-1}$ correspond to the positions for disordered polymethylene chains. The appearance of these bands suggests
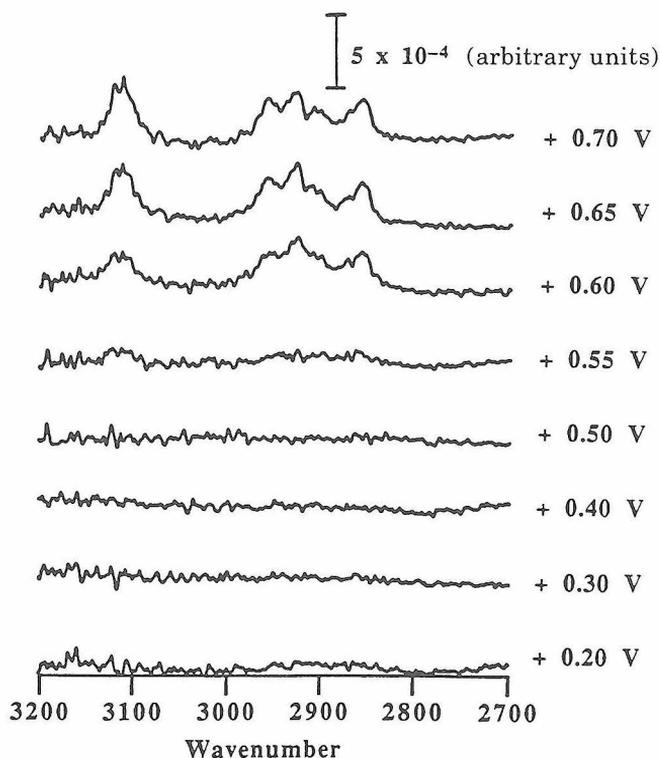
**Fig. 3.24** *In situ* differential spectra of a monolayer from $FcC_{11}SH$ at gold in $1.0\,M\,HClO_4$ between 3200 and $2700\,cm^{-1}$ as a function of applied voltage. The reference spectrum was taken at $0.20\,V$ (reproduced with permission from reference 43).

that the oxidation of the ferrocenyl moiety indicates a change in the structure of the monolayer. However, control experiments using a series of bulk ferrocene esters indicate that such changes can also be induced on the $\alpha$-methylene group by the oxidation of the ferrocenyl moiety. This finding, coupled with the low signal strength of the changes, argues against a structural change. Therefore, while we expect that changes in the structure of the monolayer should result from the redox transformation of the ferrocenyl group, the data in Figs. 3.21 and 3.22 are insufficient to support such a conclusion. Pending improvements in instrument performance may provide data that will allow a more definite interpretation. We note that similar conclusions have been reached for a structurally different monolayer system [44].

## Aluminum Nitride Thin-Film Characterization

The examples discussed above have dealt with the use of IRS to characterize organic thin films. However, the use of this technique is continuously expanding, spanning into studies of thin films of inorganic materials. One illustration of this is recent work on the characterization of aluminum nitride (AlN) films. The chemical and thermal stability of AlN films, along with their electrical, optical, and acoustic properties, have generated considerable interest in the microelectronics research area. One example is the potential use of AlN as the transducer in high-performance piezoelectric mass sensors [52]. The efficient exploitation of this material, however, requires a thorough understanding of the effects of preparative variables on the resulting acoustical properties. Typically AlN films are formed by sputtering an aluminum target with a nitrogen plasma. Interestingly, recent studies indicate that the acoustical properties of AlN are improved if hydrogen is added as a component to the nitrogen plasma. To further diagnose the role of such processing, IRS has been used to probe the composition of AlN films fabricated under various conditions as well as to study the stability of the films by monitoring changes in the film composition as a function of exposure to different environments [53, 54, 55]. IRS is an attractive probe for this application because of the wealth of information that vibrational spectroscopy provides on the chemical and physical composition of the sample. In addition reflection spectroscopy is well suited for studying thin films, the form in which AlN is typically used.

In these studies AlN films with thicknesses ranging from 8 to 40 nm were deposited on both aluminum and gold mirrors. Although reflection spectra could be obtained using either substrate, gold has the advantage of being more chemically inert than aluminum and therefore preferable as a substrate. Reflection spectra were recorded using a Fourier transform interferometer with the impinging beam incident at $\sim 80°$. The immense value of the information provided by this technique is revealed by the species identified in these spectra. For films fabricated using a pure nitrogen plasma, the most prominent features in the spectra are a band at $910\,cm^{-1}$, a longitudinal optical (LO) mode of AlN; accompanied by a shoulder for a transverse optical (TO) mode on the low-energy side of the LO mode. The LO mode is associated with the crystalline form of AlN. Importantly, a small shift of the LO band maximum with increasing film thickness was detected, suggested an increase in the amorphous character of the film. This result indicates that IRS could provide a rapid and convenient method for evaluating film quality, which is important because the performance of AlN in many applications is enhanced by higher film crystallinity.

In addition to AlN, the spectroscoic data also revealed the presence of $AlN_2$ as a component of the plasma-deposited thin film. Studies in which

the thickness of the films were varied between 8 and 40 nm and produced in a pure $N_2$ plasma indicated that the concentration of $AlN_2$ reached a maximum at 20 nm and dropped to a negligible level at 40 nm. In contrast, the absorbance feature for $AlN_2$ in films produced in a 25% $H_2$-enriched plasma increased linearly with film thickness. Spectral bands associated with Al–H and N–H were identified in the films prepared by both processes, along with bands for O–H and C–H vibrations. These latter findings suggest that the films are contaminated to a small degree during processing, demonstrating the potential for using IR reflection spectroscopy to monitor *in situ* the composition and purity of very thin films during fabrication.

The chemical information that IRS provides can be exploited to help understand the factors that influence the chemical stability of materials. Spectra of AlN films produced with pure $N_2$ and exposed for variable amounts of time to the laboratory ambient showed clear increases in the magnitudes of the N–H vibrations. This observation supports the view that moisture from the ambient reacts with AlN to form $Al_2O_3$ and $NH_3$, the latter of which is probably bound to the AlN surface via aluminum ions. Correlations with exposure time also indicated that the magnitude of the N–H signature increased for exposures up to ~1.5 hr and then remained effectively constant. In contrast, there was not a significant decrease in the magnitudes of the AlN bands. This correlation argues that after a surface layer is hydrolyzed, the resulting $Al_2O_3$ film acts as a passivation layer toward further hydrolysis. This conclusion may account for the high stability of AlN toward further reactions with atmospheric moisture. Films produced with a hydrogen-enriched plasma and exposed to the atmosphere displayed an increase in the susceptibility to hydrolysis. In this case measurable decreases in the magnitude of the AlN vibrational bands, which were coupled with the appearance of features diagnostic of an immobilized $NH_x$ species, were reported. The decrease in the magnitudes of the AlN bands indicated about a 15% depletion of the AlN film. This technique was also used to delineate the effects of exposing the AlN films to water. In this case hydrolysis occurred to equal extents with films produced with and without hydrogen added to the plasma.

This example of the application of external reflection infrared spectroscopy demonstrates how the technique can be used to address issues in microelectronics research area. The technique can be used to check the composition of thin films and to monitor for the presence of impurities. The lattice vibrations in IR spectra provide information on morphology of the films. Also IRS can be used to study the factors that influence the reactivity films to environmental influences.

## 3.5   CONCLUSIONS AND PROSPECTUS

We have discussed applications of infrared specular reflection spectroscopy as a probe of the composition and spatial orientation of materials immobilized on a wide array of substrates. Coupled with the high level of performance of infrared instrumentation, the ability to determine via classical electromagnetic theory the experimental conditions optimal for characterizations on surfaces with a range of reflectivities opens the way to tackling characterizations previously viewed as intractable. A particularly intriguing example of such an instance is the recent characterization of the structure of a single monolayer film at the air-water interface of a Langmuir trough [56]. Though not discussed as a specific application in Section 3.4, this example further demonstrates the insight afforded by consideration of the physical optics of a reflection measurement. As further improvements in instrumentation emerge, capabilities to follow surface reaction dynamics will undoubtedly appear. Such a capability will provide a much-needed access into the molecular reaction pathways of importance to catalysis and other important interfacial processes.

## ACKNOWLEDGMENTS

## REFERENCES

1. D. L. Allara, In *Characterization of Organic Thin Films,* A. Ulman, ed. Butterworth-Heinemann, Boston, 1995.

2. M. D. Porter, *Anal Chem.,* **60**, 1143A (1988).

3. H. Ishida, *Rubber Chem. Technol.,* **60**, 497 (1987).

4. A. M. Bradshaw, *Appl. Surf. Sci.,* **11/12**, 712 (1982).

5. W. G. Golden and D. D. Saperstein, *J. Electron. Spectrosc.,* **30**, 43 (1983).

6. F. M. Hoffman, *Surf. Sci. Rep.,* **3**, 107 (1983).

7. A. Ulman, *An Introduction to Ultra-Thin Organic Films From Langmuir-Blodgett to Self-Assembly.* Academic Press, San Diego, 1991.

8. D. R. Jung and A. W. Czanderna, *Crit. Rev. Solid State Mat. Sci.*, **19**, 1 (1994).

9. A. J. Bard, H. D. Abruña, C. E. Chidsey, L. R. Faulkner, S. W. Feldberg, K. Itaya, M. Majda, O. Melroy, R. W. Murray, M. D. Porter, M. P. Soriaga, and H. S. White, *J. Phys. Chem.*, **97**, 7147 (1993).

10. R. G. Greenler, *J. Chem. Phys.*, **44**, 310 (1966).

11. W. N. Hansen, *J. Opt. Soc. Am.*, **58**, 380 (1968).

12. W. N. Hansen, In *Advances in Electrochemistry and Electrochemical Engineering*, P. Delahay and C. W. Tobias, eds. Wiley, New York, 1973.

13. J. D. E. McIntyre, In *Advances in Electrochemistry and Electrochemical Engineering*, P. Delahay and C. W. Tobias, eds. Wiley, New York, 1973.

14. D. J. Griffiths, *Introduction to Electrodynamics*, Prentice-Hall, Englewood Cliffs, NJ, 1981.

15. J. P. Hawranek, P. Neelakantan, R. P. Young, and R. N. Jones, *Spectrochim. Acta. Part A*, **32**, 85 (1976).

16. H. A. Pearce and N. Sheppard, *Surf. Sci.*, **59**, 205 (1976).

17. J. A. Stratton, *Electromagnetic Theory*. McGraw-Hill, New York, 1941.

18. M. Born and E. Wolf, *Principles of Optics*, 5th ed. Pergamon Press, Oxford, 1975.

19. E. D. Palik, ed., *Handbook of Optical Constants of Solids*. Academic Press, Orlando, 1985.

20. F. A. Jenkins and H. E. White, *Fundamentals of Optics*, 3rd ed. McGraw-Hill, New York, 1957.

21. D. L. Allara, A. Baca, and C. A. Pryde, *Macromolecules*, **11**, 1215 (1978).

22. M. D. Porter, T. B. Bright, D. L. Allara, and T. Kuwana, *Anal. Chem.*, **58**, 2461 (1986).

23. D. L. Allara and R. G. Nuzzo, *Langmuir*, **1**, 52 (1985).

24. A. N. Parikh and D. L. Allara, *J. Chem. Phys.*, **96**, 927 (1992).

25. See Chapter 8 on Raman microspectroscopy.

26. M. M. Walczak, C. Chung, S. M. Stole, C. A. Widrig, and M. D. Porter, *J. Am. Chem. Soc.*, **113**, 2370 (1991).

27. C. J. Zhong and M. D. Porter, *J. Am. Chem. Soc.*, **116**, 11616 (1994).

28. R. V. Duevel and R. M. Corn, *Anal. Chem.*, **64**, 337 (1992).

29. C. Korzeniewski and S. Pons, *Prog. Anal. Spectrosc.*, **10**, 1 (1987).

30. S. M. Stole, D. D. Popenoe, and M. D. Porter, In *Electrochemical Interfaces: Modern Techniques for In Situ Interface Characterization*, H. D. Abruña, ed. VCH, New York, 1991.

31. B. J. Barner, M. J. Green, E. I. Saéz, and R. M. Corn, *Anal. Chem.* **63**, 55 (1991).

32. W. N. Richmond, P. W. Faguy, R. S. Jackson, and S. C. Weibel, *Anal. Chem.*, **68**, 621 (1996).

33. S. Wu, *Polymer Interface Adhesion*, Marcel Dekker, New York, 1982.

34. W. G. Golden, C. Snyder, and B. J. Smith, *J. Phys. Chem.*, **86**, 4675 (1982).

35. M. K. Debe, *J. Vac. Sci. Technol.*, **21**, 74 (1982).

36. J. F. Rabolt, F. C. Burns, N. E. Schlotter, and J. D. Swalen, *J. Chem. Phys.*, **78**, 946 (1983).

37. D. L. Allara and J. D. Swalen, *J. Phys. Chem.*, **86**, 2700 (1982).

38. J. Umemura, T. Kamata, T. Kawai, and T. Takenaka, *J. Phys. Chem.*, **94**, 62 (1990).

39. T. J. Lenk, V. M. Hallmark, J. F. Rabolt, L. Haussling, and H. Ringsdorf, *Macromolecules*, **26**, 1230 (1993).

40. K. Kelley, Y. Ishino, and H. Ishida, *Thin Solid Films*, **154**, 271 (1987).

41. M. Zhang and M. R. Anderson, *Langmuir*, **10**, 2807 (1994).

42. D. D. Popenoe, S. M. Stole, and M. D. Porter, *Appl. Spectrosc.*, **46**, 79 (1992).

43. D. D. Popenoe, R. S. Deinhammer, and M. D. Porter, *Langmuir*, **8**, 2521 (1992).

44. T. Sasaki, I. T. Bae, D. A. Scherson, B. G. Bravo, and M. P. Soriaga, *Langmuir*, **6**, 1234 (1990).

45. V. K. F. Chia, J. L. Stickney, M. P. Soriaga, S. D. Rosasco, G. N. Salaita, A. T. Hubbard, J. B. Benziger, and K.-W. Peter Pang, *J. Electroanal. Chem.*, **163**, 407 (1984).

46. B. E. Hayden and A. M. Bradshaw, *Surf. Sci.*, **125**, 787 (1983).

47. N. E. Schlotter, M. D. Porter, T. B. Bright, and D. L. Allara, *Chem. Phys. Lett.*, **132**, 93 (1986).

48. C. J. Zhong and M. D. Porter, *Anal. Chem.*, **67**, 709A (1995).

49. L. H. Dubois and R. G. Nuzzo, *Annu. Rev. Phys. Chem.*, **43**, 437 (1992).

50. R. G. Snyder, S. L. Hsu, and S. Krimm, *Spectrochim. Acta. Part A*, **34**, 946 (1978).

51. R. G. Snyder, H. L. Strauss, and C. A. Elliger, *J. Phys. Chem.*, **86**, 5145 (1982).

52. R. P. O'Toole, S. G. Burns, G. J. Bastiaans, and M. D. Porter, *Anal. Chem.*, **64**, 1289 (1992).

53. U. Mazur and A. C. Cleary, *J. Phys. Chem.*, **94**, 189 (1990).

54. U. Mazur, *Langmuir*, **6**, 1331 (1990).

55. X.-D. Wang, K. W. Hipps, and U. Mazur, *J. Phys. Chem.*, **96**, 8485 (1992).

56. M. L. Mitchell and R. A. Dluhy, *J. Am. Chem. Soc.*, **110**, 712 (1988).